

The geophysical environment of Bennu



D.J. Scheeres^{a,*}, S.G. Hesar^a, S. Tardivel^b, M. Hirabayashi^c, D. Farnocchia^b, J.W. McMahon^a, S.R. Chesley^b, O. Barnouin^d, R.P. Binzel^e, W.F. Bottke^f, M.G. Daly^g, J.P. Emery^h, C.W. Hergenrotherⁱ, D.S. Laurettaⁱ, J.R. Marshall^j, P. Michel^k, M.C. Nolanⁱ, K.J. Walsh^f

^a Department of Aerospace Engineering Sciences, University of Colorado, Boulder, CO 80309, USA

^b Purdue University, 550 Stadium Mall Drive, West Lafayette, IN 47907, USA

^c Jet Propulsion Laboratory, California Institute of Technology, 4800 Oak Grove Drive, Pasadena, CA 91109, USA

^d Applied Physics Lab/Johns Hopkins University, 11100 Johns Hopkins Road, Laurel, MD 20723, USA

^e Massachusetts Institute of Technology, 77 Massachusetts Ave, Cambridge, MA 02139, USA

^f Southwest Research Institute, Boulder, CO 80302, USA

^g York University, 4700 Keele St, Toronto, ON M3J 1P3, Canada

^h Univ. Tennessee, Knoxville, TN 37996, USA

ⁱ Univ. Arizona, Tucson, AZ 85721, USA

^j NASA Ames Research Center, Moffett Field, CA 94035, USA

^k Observatoire de la Côte d'Azur, Boulevard de l'Observatoire, 06300 Nice, France

ARTICLE INFO

Article history:

Received 21 November 2015

Revised 3 April 2016

Accepted 11 April 2016

Available online 28 April 2016

Keywords:

Asteroid Bennu

Geophysics

ABSTRACT

An analysis of the surface and interior state of Asteroid (101955) Bennu, the target asteroid of the OSIRIS-REx sample return mission, is given using models based on Earth-based observations of this body. These observations have enabled models of its shape, spin state, mass and surface properties to be developed. Based on these data the range of surface and interior states possible for this body are evaluated, assuming a uniform mass distribution. These products include the geopotential, surface slopes, near-surface dynamical environment, interior stress states and other quantities of interest. In addition, competing theories for its current shape are reviewed along with the relevant planned OSIRIS-REx measurements.

© 2016 Elsevier Inc. All rights reserved.

1. Introduction

The OSIRIS-REx mission to Asteroid (101955) Bennu provides an unprecedented opportunity to thoroughly map and investigate the geophysical state of a primitive asteroid. OSIRIS-REx is a sample return mission to Bennu, launching in 2016 and returning with a sample in 2023 (Lauretta, 2015). Bennu is a B-type asteroid, which is a subclass among the larger group of C-complex asteroids. Bennu is of interest scientifically due to its primitive nature and due to its spheroidal shape with a visibly prominent equatorial ridge. These properties provide the opportunity to both evaluate the geophysical processes that may occur on and within a primitive body, and to probe the genesis of the frequently seen equatorial ridges on small asteroids. Due to its low density and apparent high porosity (when compared with analog meteorites) Bennu is likely to be a rubble-pile (Chesley et al., 2014), which adds to the scientific inter-

est of this body. Bennu is also of interest as it currently has a non-negligible probability of impact with Earth in the future (Chesley et al., 2014), and thus it is relevant to understand all aspects of this body for potential impact mitigation.

As part of the preparatory activities for the rendezvous of the OSIRIS-REx spacecraft with this asteroid, a series of scientific papers have been published that cover fundamental aspects of what is known regarding this body from Earth-based observations, summarized in Hergenrother et al. (2014). Previous papers have already discussed estimates of this asteroid's shape (Nolan et al., 2013), mass and density (Chesley et al., 2014), rotation state (Hergenrother et al., 2013), spectral signature (Binzel et al., 2015; Clark et al., 2011), photometric properties (Hergenrother et al., 2013), thermal inertia properties (Emery et al., 2014) and cosmochemical and dynamical history (Bottke et al., 2015; Lauretta et al., 2015; Walsh et al., 2013). The current paper integrates results from several of these papers in order to perform an analysis of the geophysics of this body. This study will be of use to motivate observation plans for the OSIRIS-REx mission, and once these are taken it can be used to test the limits of our ability to analyze asteroids using Earth-based observations.

* Corresponding author. Tel.: +1 7205441260.

E-mail address: scheeres@colorado.edu (D.J. Scheeres).

The quantities of interest for understanding the geophysics of Bennu and its past geophysical evolution are its shape, spin state, gravity field (including total mass), visible surface morphology and spectra, topography, and the distribution and properties of surface regolith. From these quantities one can determine the geophysical environment on and within the body, potentially detect density inhomogeneities, and compare the estimated environment with visible surface features. These also provide a physical context for better understanding and interpreting spectral and compositional observations taken of the surface. All of these can be synthesized into theories of the formation and subsequent evolution of Bennu.

The current paper will map out current understanding of this body, describe existing models for geophysical evolution currently in the literature, and review the specific measurements of the Bennu system that will be taken by the OSIRIS-REx mission and describe how these will be used to develop theories for the formation and evolution of this system. Although the fidelity of these models is currently limited, especially as compared to the fidelity of the eventual OSIRIS-REx models (Lauretta et al., 2015), it is remarkable that detailed predictions of the expected environment both on, about and within this body can be developed. It should be noted that the set of existing models of Bennu are distinguished in their completeness and detail, and thus are worthy of study independent of the pending OSIRIS-REx rendezvous and exploration activities. Study and analysis of small rubble-pile bodies such as Bennu have the potential to shape our understanding of how small bodies in the solar system are formed, how they evolve and what their ultimate fate is.

Previous missions and observations have contributed greatly to our understanding of small asteroid interiors and morphology, as reviewed in Scheeres et al. (2015). Most significant among these are the NEAR mission to Asteroid (433) Eros (Veeverka et al., 2000) and the Hayabusa mission to Asteroid (25143) Itokawa (Fujiwara et al., 2006). Main conclusions from the observations of Eros, which is about 10 km in average radius, are that this body has a remarkably uniform density distribution (Miller et al., 2002), and that it was able to transmit impact shock waves across and through the body efficiently enough to erase a subset of its craters (Thomas and Robinson, 2005). Intriguing surface features and structures were also found, some of them global, that indicate that the body may have significant subsurface features beneath the blanket of regolith that covers the body (Cheng et al., 2001; Procter et al., 2002; Robinson et al., 2002). Itokawa, which is much smaller with a 160 m mean radius, provided a first clear view of a rubble-pile body and showed itself to be comprised of rocks with a size distribution that approximately followed a d^{-3} size distribution, where d is the rock diameter, across its surface down to the meter level (DeSouza et al., 2015; Mazrouei et al., 2014; Michikami et al., 2008), with an indication of a less steep distribution (between -2 and -3) at the sub-meter level (Noviello et al., 2014). Further, the sample obtained from its surface also showed a similar size distribution, but ranged down to micron sized grains (Tsuchiyama et al., 2011). Surface properties of Itokawa were measured during one of the sampling attempts (Yano et al., 2006) and the existence of surface flow of regolith was shown based on analysis of regional imaging (Miyamoto et al., 2007) and a global assessment of surface roughness (Barnouin-Jha et al., 2008) and block aspect ratio investigations (Michikami et al., 2010). The total mass of Itokawa was measured based on imaging and lidar measurements (Abe et al., 2006). Unfortunately, precise Doppler tracking of the spacecraft when it was in close proximity to Itokawa has not been published, which has prevented the estimation of any gravity field coefficients, preventing analysis of its interior mass distribution (although there has been speculation about possible density inhomogeneity in this body (Lowry et al., 2014), which was critically assessed in Scheeres et al. (2015)). Thus, despite the many

fundamental advances in understanding that arose from these missions, key insight into some geophysical aspects of small bodies remain opaque.

One specific question of interest for Bennu revolves around how its equatorial ridge formed, as this will provide direct insight into the shape evolution of such rubble-pile bodies. It will potentially even inform us of the process by which binary asteroids are formed, as an equatorial ridge is a common feature on primaries of small binary systems, based on radar observations (Benner et al., 2015). The ridge is used as motivation in this paper, given that it is the most prominent feature in the radar-derived shape model correlated to the geophysical evolution of Bennu. There will be many additional questions of interest that arise once rendezvous with Bennu occurs, however to understand these features will likely involve the same methods and measurements for understanding the ridge. Key measurements that will inform this investigation include the surface topography and morphology, surface heterogeneity of material and its size distribution properties, crater morphologies and number, the bulk density and any constraints on density inhomogeneities within the body, the presence or absence of an excited rotation state, and any evidence for surface landslides, material infall or uplift of the surface. In sum, the integrated observations of this body will provide the essential foundations for understanding how it arrived at its current state. The current paper sets up a number of different analyses and interpretations of the existing data, and hopefully will serve as a springboard for the detailed investigation of this body once the OSIRIS-REx spacecraft has its rendezvous with Bennu in 2018.

The paper is split into the following sections. Section 2 reviews the existing models for this body with a focus on the essential values that influence our understanding of the Bennu geophysical environment. Section 3 reviews the derived models essential for our analysis. Section 4 provides a series of geophysical calculations that define the possible state of the body's surface and interior, and which place limits on possible past states that this body may have had. Section 5 focuses more narrowly on describing the array of current theories for the genesis of the current Bennu shape. Then Section 6 covers the primary measurements that will be made and indicates how these can be applied to discern between some of these competing theories. Finally, the Conclusion section provides a brief review of the results.

2. Defining models and current values

There is a remarkable amount of current knowledge on Bennu, due to a combination of many different observation campaigns. These include astrometric, photometric, radar, thermal infrared, and spectral observations of this body that have been reported elsewhere (Binzel et al., 2015; Emery et al., 2014; Hergenrother et al., 2013; Nolan et al., 2013). These observations have been combined through a large-scale effort into a model of good fidelity that enables the current study, and helps to formulate the appropriate questions and investigations to pursue at this body. In the following, the major aspects of this body are recounted in a combined manner, although many of these specific elements came from disjoint methods of observation.

2.1. Surface constraints

Measurements of the thermal spectral flux of Bennu as a function of rotation with the Spitzer Space Telescope point to a fairly homogeneous, relatively fine-grained surface estimated to be of size 0.1–1 cm (Emery et al., 2014). Variations of disk-integrated thermal flux with rotation are consistent with being entirely due to shape-induced changes in cross-sectional area, suggesting that the physical properties of the surface do not vary dramatically

Table 1

Bennu shape and geometrically defined properties. Several of these are taken from Nolan et al. (2013), although the center of mass and moments of inertia are computed from the shape model assuming a homogeneous density distribution.

Mean radius	246 ± 10 m
Equatorial diameter limits	$565, 535 \pm 10$ m
Polar diameter	508 ± 52 m
Volume	$6.23 \pm 0.06 \times 10^7$ m ³
Center of mass r_c	$0.043, -0.005, 0.002$ m
Mass normalized moments of inertia	
I_{min}	2.32447×10^4 m ²
I_{int}	2.41532×10^4 m ²
I_{max}	2.60664×10^4 m ²

longitudinally. The low visible geometric albedo of 0.045 ± 0.005 constrains the surface composition, and is consistent with CM-carbonaceous-chondrite-like material. With an average thermal inertia of 310 ± 70 J m⁻² s^{-1/2} K⁻¹, Bennu is inferred to support a regolith with an abundance of sub-cm-sized grains. This thermal inertia, analyzed using laboratory calibrations and a semi-empirical formalism for a mono-disperse grain distribution (Gundlach and Blum, 2013), suggests a characteristic grain size of ~ 0.35 cm. It is not possible in this computation to separate porosity from grain size. Considering a range of regolith porosities from 0.6 to 0.1 and the full 1-sigma range in thermal inertia uncertainties results in a range of potential grain sizes of 0.17–0.95 cm. Potential rotational heterogeneity in thermal inertia of ± 60 (SI units) would suggest a variation of only 0.05 cm in characteristic grain size. It is also significant to note that observations by Binzel et al. (2015) show evidence for the equatorial ridge of Bennu having a redder spectral slope than the poles, indicating a latitudinal variation.

2.2. Shape model

The overall shape of Bennu was determined through radar and lightcurve observations, as reported in Nolan et al. (2013). The basic parameters of the body's shape are summarized in Table 1. The surface resolution of the resultant shape model is at the few decameter level and the radial features are uncertain at the decameter level – although there is a large uncertainty in the length of the polar axis. The shape model consists of 2692 triangular facets which are in general uniformly distributed, yielding an average area of 290 m² per facet, corresponding to a square with side lengths of 17 m. Thus, with the final expected shape resolution of less than 1 m, the model estimated by OSIRIS-REx will provide orders of magnitude of improvement over the current model, yielding significant insight into the structure of a primitive asteroid at unprecedented resolution. Uncertainties in the size of the shape model are not accounted for in the current discussion, in part because the size, density and spin rate of a body can be essentially tied together through the normalized spin parameter introduced later in Section 4.4. This being said, the greater than 10% uncertainty in the polar dimension of the body could substantially change important elements of the asteroid's geometric and geophysical properties should it lie at either extreme.

2.3. Bennu spin state

The spin rate of Bennu has been measured, through photometric observations, to be 4.29746 ± 0.002 h, with the corresponding spin rate of $\omega = 4.0613 \times 10^{-4} \pm 1.9 \times 10^{-7}$ rad s⁻¹ (Hergenrother et al., 2013). The spin pole of the body is retrograde with an obliquity of $\sim 180^\circ$. While this body is a candidate for the Yarkovsky–O'Keefe–Radzievskii–Paddack (YORP) effect, which would be indicated by a steady change in the spin period of this asteroid, the

presence of this effect has not been detected as of yet. Also significant is that a non-principal axis rotation state has not been detected for this body, although one cannot be ruled out. Based on ground observations alone it is unlikely that any nutation angle less than $\sim 10^\circ$ could be detected by ground observations alone, though such a large spin pole deviation would be easily detectable once the body is resolved with imaging.

2.4. Mass and density

A significant achievement from the observation campaigns was the determination of the mass of Bennu, through determination of its density and volume (Chesley et al., 2014). This was enabled through a combination of astrometric, radar and thermal observations. The density was estimated to be 1260 ± 70 kg m⁻³, indicating a likely rubble-pile body. This analysis takes the $\pm 3\sigma$ uncertainties found for the density. Specifically, the minimum density considered is 1050 kg m⁻³, the maximum density is 1470 kg m⁻³ and the nominal density is 1260 kg m⁻³. The associated nominal total mass and gravitational parameter is 7.8×10^{10} kg and $\mu = GM = 5.2$ m³ s⁻², respectively. Knowledge of the density and GM is key, as it opens up a range of more detailed and relevant studies for this body.

2.5. Porosity

A fundamental geophysical parameter that can be calculated for Bennu is its inferred porosity. This is calculated from the density and the inferred grain density of the material that makes up the body. For the nominal density estimate of Bennu the porosity is inferred to be $40 \pm 10\%$, based on an assumed grain density of 2100 kg m⁻³, which is still quite uncertain (Hergenrother et al., 2014). The interpretation of this parameter is important but is not well understood for asteroids as of yet and is one of the objectives for analysis of the returned sample. Specific questions are whether the body has large voids within it or if it has a more evenly distributed porosity. This is especially called into question by the radar measurements results which indicated a surface porosity of 20% (Lauretta et al., 2015; Nolan et al., 2013). The physical interpretation of these radar measurements has not been tested for asteroidal bodies, and thus understanding these measurements will also be an item of interest. As the depth of this porosity is not well constrained it is not considered in the current paper, which is more focused on the detection of global inhomogeneities. Comparison of the estimated gravity field with the shape model-derived constant-density gravity field is one such method which can be used to detect such global density inhomogeneities and is discussed in Section 6.4.

3. Derived models

Given the above constraints and measurements of Bennu, these can be combined into specific models for analysis of this system. This involves understanding the mass distribution of the asteroid, constraints on its possible spin state, definition of the geopotential of the asteroid and its related properties, and finally the computation of its gravity field and expected variations that it could have.

The following analyses assume that the density is uniformly distributed through the shape model. This is certainly reasonable, given the mass distribution homogeneity found for Eros (Konopliv et al., 2002; Miller et al., 2002), although we do note that theories for the ridge formation on Bennu (discussed later in section) predict non-uniform density distributions. Further, Bennu has a much smaller size (almost two orders of magnitude below that of Eros) and is most likely a rubble pile while Eros is most likely not, thus direct comparisons with Eros have a high degree of uncertainty.

Table 2

Coordinate shift and rotation to center the Bennu shape from Nolan et al. (2013) at its center of volume and orient it along the constant density principal axes of inertia.

Center of mass shift (m)	0.043	−0.005	0.002
Frame rotation	0.999999	0.001695	0.000063
	−0.001695	0.999999	−0.000001
	−0.000063	0.000001	0.999999

Density inhomogeneities are discussed at several points of the paper.

3.1. Mass distribution

Given the Bennu shape and constant density assumption the different mass moments for this body can be computed. These include the total mass, center of mass vector and inertia dyad. All of these are computed by integrating over the mass distribution of the body.

$$M = \int_{\mathcal{B}} dm \quad (1)$$

$$\mathbf{r}_c = \frac{1}{M} \int_{\mathcal{B}} \boldsymbol{\rho} dm \quad (2)$$

$$\bar{\mathbf{I}}_c = \frac{1}{M} \int_{\mathcal{B}} [\rho^2 \bar{\mathbf{U}} - \boldsymbol{\rho} \boldsymbol{\rho}] dm - [r_c^2 \bar{\mathbf{U}} - \mathbf{r}_c \mathbf{r}_c] \quad (3)$$

In the above \mathcal{B} denotes the Bennu shape, the vector $\boldsymbol{\rho}$ is the integration variable across the Bennu shape, the mass differential $dm = \sigma dV$ which is the density times the differential volume, a bold-faced quantity denotes a vector and boldface with an overline denotes a dyad. Specifically, \mathbf{r}_c is the center of mass vector, $\bar{\mathbf{I}}_c$ is the mass-normalized inertia dyad relative to the center of mass, $\bar{\mathbf{U}}$ is the unity dyad and the quantity $\mathbf{r}_c \mathbf{r}_c$ is a dyadic product of the center of mass vector. We do not assume that the shape model is at the center of mass or in a principal axis frame.

Table 1 lists the main geometrical elements of the shape model, as defined above. The principal moments of inertia are the eigenvalues of the inertia dyad $\bar{\mathbf{I}}_c$. The mean diameter is defined as the diameter of a sphere with equal volume to the Bennu shape. The uncertainties are based on quoted uncertainties from Nolan et al. (2013). The non-zero center of mass (which is equivalent to the center of figure for a constant density) arises as the delivered shape model was not fully centered at this point. For reference, Table 2 defines the shift and rotation applied to the published shape model to center it at the center of mass and orient it along a principal axis frame. During the mission the shape model coordinate frame will in general be aligned with the body center of mass.

3.2. Spin state models

For the current analysis the body is assumed to be in a uniform spin state, rotating about its maximum moment of inertia. Given the computed inertia dyad, the spin vector must lie along the eigenvector corresponding to the maximum moment of inertia. If not in a principal axis frame, the eigenvector \mathbf{u} must be found such that

$$\bar{\mathbf{I}} \cdot \mathbf{u} = I_{\max} \mathbf{u} \quad (4)$$

Then the angular velocity vector of the asteroid is $\boldsymbol{\omega} = \omega \mathbf{u}$, assuming that \mathbf{u} is a unit vector and ω is the spin rate.

Given the moments of inertia and total spin rate it is possible to identify the limiting precession and nutation period for this body, applying asymptotic formula for a complex rotator as its nutation angle approaches 0 (see, e.g. Scheeres, 2012b). Doing so with the Bennu model parameters predicts that if it were offset slightly from a uniform rotation it would have a precession period of 3.9 h and a nutation period of 43.0 h. The precession period is the time it takes for the pole of the asteroid to rotate in inertial space. The nutation period is the time it takes the equatorial plane to go through an entire cycle of its nutation angle oscillation and equals the period of the angular velocity vector in the body-fixed frame if perturbed from the maximum moment of inertia axis. The difference of these two related frequencies yields the observed body spin period of ~ 4.29 h, and in the limit as the nutation angle goes to zero these two frequencies combine into the spin period. Due to this it is difficult to differentiate between uniform rotation and a complex rotation if a small offset between the spin pole and the angular momentum vector exists. Once images of the asteroid are resolved, however, any complex rotation should become much more visible. With projected accuracies in the shape model of less than a meter, it should be possible to detect nutation angles of less than 0.2° .

A separate, but highly relevant question for the Bennu spin rate, is the magnitude of the Yarkovsky–O’Keefe–Radzievskii–Paddack (YORP) effect. Given the highly accurate model for Bennu that will be developed, added to the long baseline over which it has been observed (Hergenrother et al., 2013), provides an excellent opportunity to measure this effect for Bennu.

A formal calculation of the normal YORP rotational acceleration for Bennu predicts a change of -6×10^{-3} degrees/day/year, but this value is highly uncertain due to the inherent challenges of accurate YORP modeling, with the YORP models of Itokawa a case in point. While Itokawa has a detected YORP acceleration (Lowry et al., 2014), it is certainly not consistent with the classical model of this effect (Breiter et al., 2009; Scheeres et al., 2007), with the deviation likely either due to internal density inhomogeneities (Lowry et al., 2014; Scheeres and Gaskell, 2008) or due to thermal effects acting on surface boulders (Golubov and Krugly, 2012; Golubov et al., 2014; Ševeček et al., 2015). While not directly considered to be a geophysical effect, the YORP effect potentially has a huge influence on the geophysical evolution of an asteroid such as Bennu. In particular, it lies at the heart of most theories regarding the shape evolution of Bennu and the formation of its ridge, and motivates the study of past possible spin rates for this body.

It is feasible for the YORP effect to be measured prior to rendezvous, given past and planned observations of Bennu. Sparse photometric lightcurve observations of Bennu were obtained over the past 16 years. These observations consist of partial lightcurves from 1999 (Krugly et al., 2002), complete rotations on four consecutive nights in 2005 (Hergenrother et al., 2013), and complete though low S/N lightcurves with HST in 2012 (Lauretta et al., 2015). Additional complete observations are planned for 2017–2018. Bennu will be faint at that time requiring observation with HST and/or large aperture ground-based telescopes. The combination of these remote observations in combination with OSIRIS-REX observations should allow the detection of YORP induced changes to the rotation period.

During the close-proximity phase of the mission the spin acceleration of Bennu will be closely tracked to evaluate any variations from the measured secular value. In addition, the full model of Bennu’s surface, photometric properties and thermal response will be combined to determine the fidelity to which the measured YORP effect can be matched with models. This activity could potentially resolve the large ambiguities in current YORP predictions.

3.3. Geopotential

The fundamental expression that drives all of the significant computed quantities across and within the body is the geopotential. This mathematical function is classically defined as the combined gravitational potential energy function plus the effective contribution from the uniform spin of the body about its maximum moment of inertia. The geopotential, as defined here, assumes that there is no spin offset away from the maximum moment of inertia, which then makes the geopotential a time invariant quantity. Should an offset exist between the body's rotational angular momentum and maximum principal moment of inertia, this function will become time-periodic in the body-fixed frame, due to the time-periodic nature of non-uniform, torque-free rotational motion in a body-fixed frame.

The geopotential is a significant quantity for a number of reasons. First, it documents the relative energy across and within the body, and can be directly related to the stress that a spinning body experiences internally. Second, it is a conserved quantity for the conservative dynamical motion of a particle in the body-fixed frame (when added to the kinetic energy relative to the body-frame). Third, it can be used to compute the accelerations acting on a particle in the body-fixed frame. In these contexts the geopotential $V(\mathbf{r})$ is sometimes called the amended potential and defined as

$$V(\mathbf{r}) = -\frac{1}{2}\omega^2(\mathbf{r} - \mathbf{r}_c) \cdot [\bar{\mathbf{U}} - \mathbf{u}\mathbf{u}] \cdot (\mathbf{r} - \mathbf{r}_c) - U(\mathbf{r}) \quad (5)$$

$$U(\mathbf{r}) = \mathcal{G} \int_B \frac{dm(\boldsymbol{\rho})}{|\mathbf{r} - \boldsymbol{\rho}|} \quad (6)$$

where \mathbf{r} is the position of a particle in the body frame, \mathbf{r}_c is the center of mass of the body, ω is its assumed uniform spin rate, \mathbf{u} is the unit vector which lies along the maximum moment of inertia of the body, $U(\mathbf{r})$ is the gravitational force potential evaluated at a given location \mathbf{r} , $\boldsymbol{\rho}$ is the location of a mass element dm in the mass distribution defined by B , and \mathcal{G} is the gravitational constant.

Note that the spin component is measured relative to the center of mass, while the gravitational force potential is not necessarily measured from the system center of mass. These generalities are removed now, but have been included up to this point as the shape model need not be aligned with center of mass or principal axis frames. If, however, the shape is centered at the center of mass and aligned with the principal axes (specifically, if the maximum moment of inertia is taken along the z axis) the geopotential takes on the simpler form

$$V(\mathbf{r}) = -\frac{1}{2}\omega^2(x^2 + y^2) - U(\mathbf{r}) \quad (7)$$

where $\mathbf{r} = x\hat{\mathbf{x}} + y\hat{\mathbf{y}} + z\hat{\mathbf{z}}$ is the position of a particle in the body-fixed frame measured from the center of mass, with the unit vectors $\hat{\mathbf{x}}$, $\hat{\mathbf{y}}$ and $\hat{\mathbf{z}}$ defined along the minimum, intermediate and maximum moments of inertia, respectively.

The negative gradient of the geopotential defines the acceleration that a particle will experience relative to the body-fixed frame, and thus can be used directly to compute items such as surface accelerations and slopes. When evaluated in the interior of the body, it provides the body force component of the loading. The geopotential can also be used to define the equations of motion for the ballistic motion of a particle in a body-fixed frame:

$$\ddot{\mathbf{r}} + 2\boldsymbol{\omega} \times \dot{\mathbf{r}} = -\frac{\partial V}{\partial \mathbf{r}} \quad (8)$$

where $\dot{\mathbf{r}}$ and $\ddot{\mathbf{r}}$ are the velocity and acceleration of the particle in a body-fixed frame rotating with an angular velocity $\boldsymbol{\omega}$ about its maximum moment of inertia.

For a uniform rotator, the geopotential also forms a conserved quantity analogous to energy in the rotating frame

$$C = \frac{1}{2}v^2 + V(\mathbf{r}) \quad (9)$$

where v denotes the magnitude of the velocity vector relative to the rotating frame. Taking the time derivative of this expression and substituting Eq. (8) shows that $dC/dt = 0$. This quantity is often called the Jacobi integral of the system and the quantity C the Jacobi energy.

This expression also provides a sharp bound on where a particle can travel in the body frame as a function of its energy. Rewriting the energy integral as $C - V(\mathbf{r}) = \frac{1}{2}v^2$ one can note the inequality

$$C - V(\mathbf{r}) \geq 0 \quad (10)$$

This allows for regions of possible motion to be delimited as a function of the Jacobi energy, and is applied later in this paper.

3.4. Gravity field

One item of significant interest, but with no current information, is the internal density distribution of this body, which is encoded in the body's gravity field. While constant density gravity field coefficients can be computed, it is only once the gravity field of Bennu is measured that explicit comparisons can be made in order to detect internal density non-uniformities (Scheeres et al., 2000; Takahashi and Scheeres, 2014a). In this paper the constant density gravity field is either computed directly from the shape model using the technique by (Werner and Scheeres, 1997) or with spherical harmonics using gravity field coefficients computed directly from the shape model with a constant density distribution assumption (Werner, 1997), a severe limitation which will be corrected once the actual gravity field is estimated. Despite this, it is important to understand the limitations of the gravity field descriptions that will be used to estimate and describe the Bennu gravity field. Thus in the following we discuss the accuracy to which the externally measured gravity field can be mapped to the surface of the body, what the nominal gravity field of Bennu currently is (based on a constant density assumption and the current shape), and what variations can be expected in the actual gravity field due to shape and density distributions.

3.4.1. Surface computation of the gravity field

For understanding the geophysics of Bennu a key computation is to map the estimated gravity field of that body to its surface. However, due to the way in which the gravity field is estimated and other limitations the evaluation of the surface gravity field is not a simple question. Previous research has investigated multiple approaches to mapping a measured gravity field to the surface. These alternate descriptions include ellipsoidal harmonics (Garmier et al., 2002), interior spherical harmonic expansions (Takahashi et al., 2013), and various other approaches (Geissler et al., 1996; Herrera-Sucarrat et al., 2013; Takahashi and Scheeres, 2014b). While these approaches are not reviewed in the current paper, it is relevant to present what the challenges are in performing this mapping.

The constant density polyhedron gravity field computation has a significant advantage as it can be computed in closed form and evaluated up to and beneath the surface consistently (Werner and Scheeres, 1997). Thus, this approach is used for computing all surface gravity field evaluations in the current paper. However, this approach is not valid for the true measured gravity field of Bennu, as it is likely that there will be inhomogeneous density distributions within the body, which will invalidate the simple use of the polyhedron model.

The estimated spherical harmonic field contains all the appropriate information on the density distribution, but it is limited

Acceleration Errors for the 4th-Order Spherical Harmonic Gravity Field

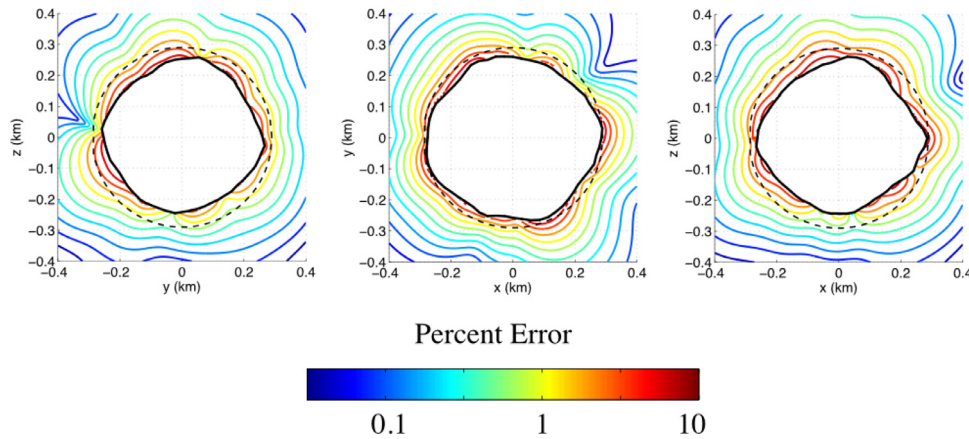


Fig. 1. Error between the spherical harmonic expansion gravity field and the exact constant density polyhedron gravity field evaluated across three mutually orthogonal planes of Bennu. Dashed line is the circumscribing sphere and the black line is the shape at the cross section.

in that it is only properly defined outside of the circumscribing sphere about the body (called the Brillouin sphere), and the spherical harmonic field diverges from the true field when within this bounded region. Fig. 1 shows this graphically, by plotting the degree of error in the acceleration computation across three planes chosen along the principal axes of inertia of the body. For a 4th degree and order gravity field the errors grow up to 10% for the exterior spherical harmonic gravity field as compared to the exact, constant density gravity field. The errors are due both to the use of a spherical harmonic expansion within the Brillouin sphere and the use of a truncated expansion.

An important issue is the conversion of measured gravity field coefficients into a gravity field descriptor that can be mapped to the surface of a body, which was researched in detail in Takahashi and Scheeres (2014a); Takahashi et al. (2013). The current paper does not delve into these issues and instead relies on the constant density assumption which allows for the direct use of the polyhedron field and its related conversion to the spherical harmonic coefficients. Such mappings are being planned for using the measured data as an accurate representation of the gravity field, and will be described in later publications.

For a nearly spherical body such as Bennu the divergence of the gravity field is not as dramatic as for strongly distended bodies. Thus, while the surface gravity field will always diverge from the truth when evaluated at the surface, the behavior with increasing degree and order acts as an asymptotic series, with increasing precision to a certain degree and order and divergence occurring at higher degrees and order. Fig. 2 shows this explicitly, with the maximum error at the surface in the spherical harmonic gravity field being minimum at degree and order 10. Measurement of the gravity field up to this level is not possible for the current OSIRIS-REx mission design and would require an extended period of orbits with very low altitudes. Due to the inherent dynamical instability of such orbits about small asteroids (Scheeres, 2012a) these are not currently being considered, although a decrease in orbit altitude from 1 km is being discussed.

3.4.2. Spherical harmonic gravity field

Despite its convergence issues close to the body, the spherical harmonic field is well suited for estimation purposes Kaula (1966),

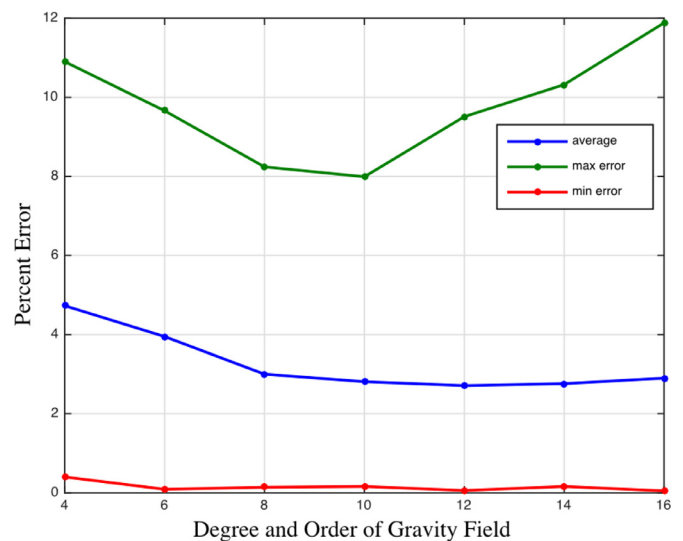


Fig. 2. Minimum, maximum and average error of the spherical harmonic gravity field mapped onto the surface of Bennu. The spherical harmonic expansion is a divergent asymptotic series, with a minimum error at a finite order of expansion.

and provides a direct measurement of the mass distribution as represented in the gravity field coefficients that are estimated by tracking the spacecraft when in orbit about the body. Independent of the practical issues of estimation and representation, the spherical harmonic coefficients are of interest as they individually have unique signatures that act on the orbital evolution of particles about these bodies. As such, it is useful to present the gravity field coefficients up through degree and order 4, and provide some discussion associated with them. Table 3 shows these coefficients, which have been computed in a reference frame that is centered at the center of volume of the shape and oriented along the principal moments of inertia. Due to the choice of this frame the first degree and order terms are zero and the second degree and order terms are all zero except for C_{20} and C_{22} . In this field the zonal gravity field terms are relatively large, with the C_{40} term having the same order of magnitude as the C_{20} term and C_{30} having a value half of

Table 3

Bennu gravity field coefficients for the constant density shape (Nolan et al., 2013). The frame is centered at the center of figure and aligned with the principal moments of inertia. The coefficients are Kaula normalized and are computed for a reference radius of 245.887 meters, which is the radius of the sphere with equivalent volume as the shape model.

Degree n	Order m	C_{nm}	S_{nm}
0	0	1	–
1	0	0	–
1	1	0	0
2	0	–0.017511	–
2	1	0	0
2	2	0.005819	0
3	0	0.005610	–
3	1	0.001544	0.001539
3	2	0.000111	0.000064
3	3	0.002671	–0.000920
4	0	0.010250	–
4	1	0.000431	0.001857
4	2	–0.002195	0.000767
4	3	–0.001076	0.000097
4	4	0.002115	0.003083

these. This is to be contrasted with the Earth's gravity field where the magnitudes of C_{30} and C_{40} are orders of magnitude less than C_{20} . Even though the magnitude of the coefficients may be similar, the gravitational force they generate are still much different, with the ratio of the magnitudes of attraction from C_{20} and C_{40} being on the order of 16 at the nominal radio science orbit of 1 km.

3.4.3. Expected uncertainties in the gravity coefficients

Although precisely computed from the current shape model, the gravity field coefficients are not very certain due to the overall uncertainty in the asteroid shape model and the density distribution. Thus it is relevant to compute the analog of a Kaula rule (Kaula, 1966) for this body in order to develop realistic bounds on what the possible variation in the true gravity field will be. In McMahon et al. (2015) a Kaula rule is developed by taking the current shape model and applying systematic and correlated shape variations that are allowed within the shape model uncertainties. It was found that the traditional Kaula rule, which makes no distinction between zonal, tesseral and sectorial coefficients, needs to be updated to account for zonals separately. This is due to their overall larger values, which is directly correlated to the rotationally symmetric yet strongly oblate shape.

To find an analog Kaula rule for Bennu, we generated 150 random shapes by perturbing the vertices of Bennu's nominal shape model with up to ± 15 m radial dispersions (which is consistent with the radar data accuracy (Nolan et al., 2013)), while different correlation lengths of 300 m, 150 m, and 50 m were used (50 shapes for each perturbation length). The correlation length controls how smooth the variation is between individual vertices: a long distance will make the perturbations affect large portions of the body, effectively reshaping the whole body, while shorter perturbation lengths will allow for more localized variation. Moreover, an additional 100 shapes were generated starting from a higher resolution shape model and with correlation lengths of 50 m and 25 m (50 shapes for each perturbation length), thus yielding a total of 250 random shapes. Each shape used a constant density distribution and the JPL Small-Body Dynamics Toolkit (Broschart et al., 2015) to compute the gravity harmonic coefficients up to degree 12 using the reference radius from Table 3.

Since the zonal coefficients C_{n0} were significantly larger than the other coefficients, a separate Kaula rule was fit as follows:

$$C_{n0} \sim \frac{K_{\text{zonal}}}{n^2}, \quad \sqrt{\frac{\sum_{m=1}^n (C_{nm}^2 + S_{nm}^2)}{2n}} \sim \frac{K_{\text{rms}}}{n^2}. \quad (11)$$

Table 4

Kaula rule best fit and upper bound parameters.

	K best fit	K upper bound
Zonal	0.084	0.183
RMS	0.025	0.043
Max	0.052	0.104

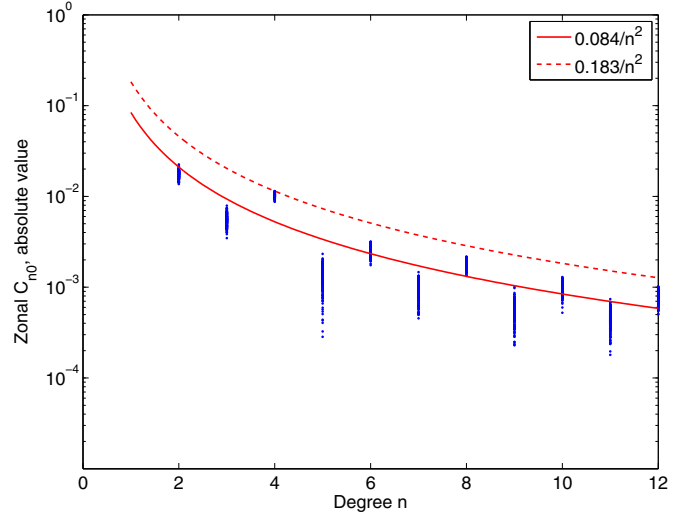


Fig. 3. The blue dots are the zonal coefficients for 250 random shapes of Bennu. The solid curve is the best fit $1/n^2$ power law, while the dashed curve is an upper bound $1/n^2$ power law.

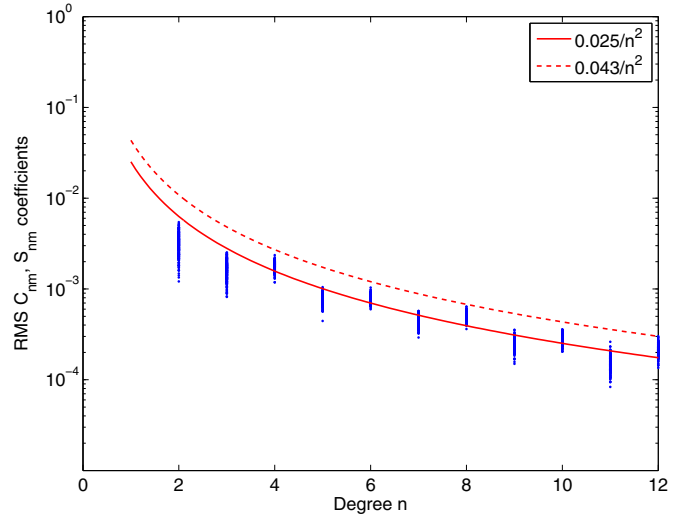


Fig. 4. The dots are the RMS values $\sqrt{\sum_{m=1}^n (C_{nm}^2 + S_{nm}^2)/(2n)}$ for 250 random shapes of Bennu. The solid curve is the best fit $1/n^2$ power law, while the dashed curve is an upper bound $1/n^2$ power law.

To obtain a conservative estimate for the non-zonal coefficients we also considered a Kaula constant using the maximum values at each degree

$$\max(|C_{nm}|, |S_{nm}|)_{m=1,\dots,n} \sim K_{\text{max}}/n^2. \quad (12)$$

Table 4 shows the best-fit Kaula rule parameters and their upper bounds for the three different cases. The values of K reflect the fact that zonal coefficients are significantly larger than non-zonal ones.

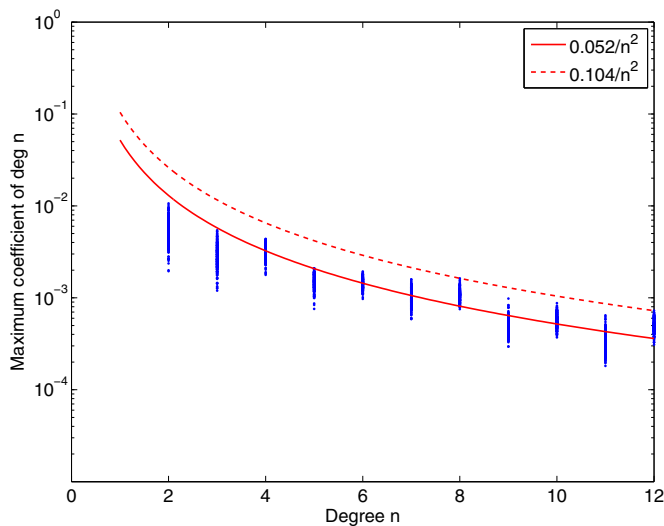


Fig. 5. The dots are the values of the maximum gravity coefficients for a fixed degree n , i.e., $\max(|C_{nm}|, |S_{nm}|)_{m=1, \dots, n}$, for 250 random shapes of Benu. The solid curve is the best fit $1/n^2$ power law, while the dashed curve is an upper bound $1/n^2$ power law.

Figs. 3–5 show the zonal and non-zonal coefficients (RMS and max) for the 250 random shapes as well as best fit and upper bound $1/n^2$ power laws. Though all the 250 shapes were considered together, the results are not significantly different among the subsets characterized by different shape resolutions and perturbation lengths.

Variation in the gravity field due to several different inhomogeneous mass distributions in the nominal Benu shape model was also investigated. Three different mass distributions were tested, a core model, a surface model, and a torus model. These distributions are pictured in Fig. 6. In each case, the two volumes in the body have their densities adjusted so that the total mass of the body stays constant. The density was varied $\pm 250 \text{ kg m}^{-3}$, so that the actual density varied between 1010 and 1510 kg m^{-3} . The key mass distribution being represented here is whether the equatorial bulge could be over or under-dense, as could the core or surface based on the location of regolith, how packed the regolith is, and how many voids are present within the body. These density distributions capture the main effects of these distributions (Takahashi and Scheeres, 2014a). For this range of density values and interior models, the resulting variation in the gravity coefficients is within the range of variation given by the Kaula rule derived from the shape modifications discussed above. Therefore we assume that this Kaula rule can be used to represent variation in both the shape and density for these types of density models. The Kaula rule will, in turn, provide an envelope of possible values for

the Benu gravity field that can be used for setting the expected a priori uncertainties.

4. Geophysical calculations

Given these data and derived models a range of quantities can be defined that describe the geophysical environment of Benu. These are mostly applications of the geopotential and its derivatives in various situations, mapped onto the surface. We start with the geopotential of this body, which can then be applied to find the surface accelerations, the surface slopes, the structure of motion close to Benu and finally be used to evaluate the interior stress state of the body. Methods for many of these computations are provided in Scheeres (2012b), and additional references are given where needed. These calculations use the nominal Benu shape model, however it is noted that some of the computed quantities will depend sensitively on what the actual, final model is. Exploration of these variations is not feasible in the current paper, however, what is perhaps more significant is the variation of these computed quantities with the bulk density of the asteroid, which is discussed in detail. First some definitions are introduced to distinguish between the geometry of the shape and surface and its geopotential.

4.1. Geometric and geopotential topography

For planetary bodies the direction of changing altitude is generally strongly correlated with the direction of changing geometry of the surface. Thus, if the radius of the surface is increasing in a given area, this is directly related to an increase of potential energy and thus a change in the relative altitude. On a small body surface with rapid rotation, however, this correlation does not occur in general. Fig. 7 explicitly shows the change in radius across the surface of Benu (which we call “geometric altitude”) as compared to the change in the geopotential (which we call “geopotential altitude” and which is defined below). Here both are measured from their minimum value. It is clear that geometric changes in the surface are quite uncorrelated with changes in the geopotential, and give a stark motivation for defining these concepts carefully. This arises due to the large rotational component in the geopotential.

Similar issues can arise with respect to the orientation of the body’s surface in terms of the geopotential or local acceleration field. For larger planetary bodies there is generally a strong correlation between the relative orientation of a body’s surface and the direction of greatest increase or decrease in geopotential, something which again does not exist for a body such as Benu. This can create confusion by mixing together two separate quantities with one terminology. For example, on a planetary body such as the Earth the relative orientation of the surface (measured as the angle between the local tangent plane and the plane perpendicular to the radius to the center of Earth) and the direction of greatest

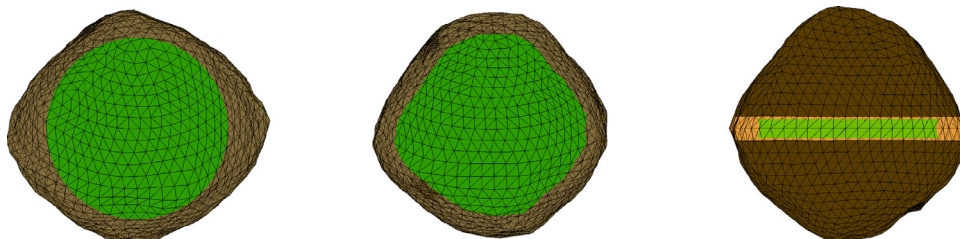


Fig. 6. Three inhomogeneous mass distribution models tested: a 200 m radius spherical core (left); a 50 m deep surface layer (middle); and a torus model approximately 50 m deep (right).

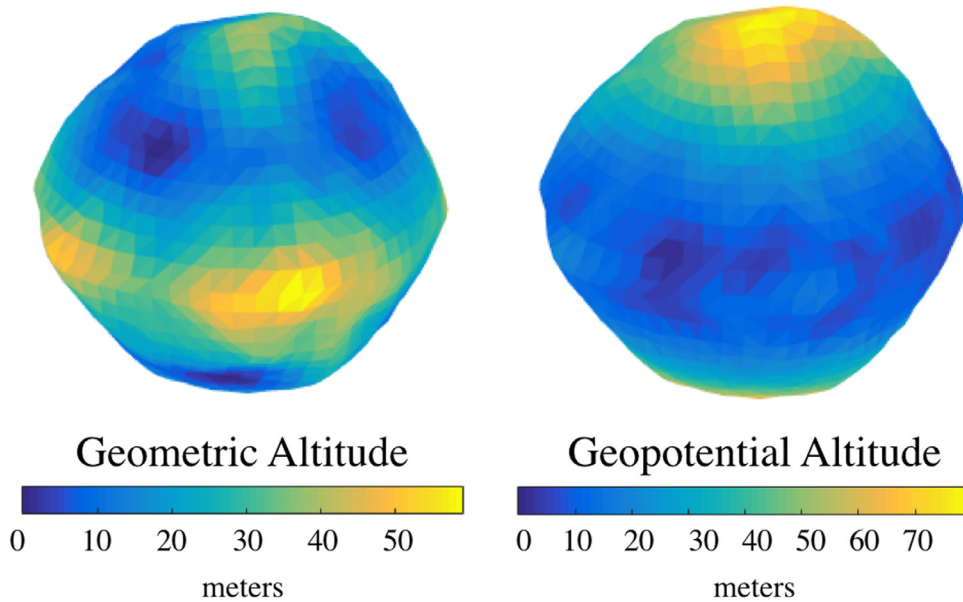


Fig. 7. Geometric and geopotential altitudes across Benu. Geometric altitude is measured from the minimum radius value of the shape while geopotential altitude is measured from the minimum geopotential.

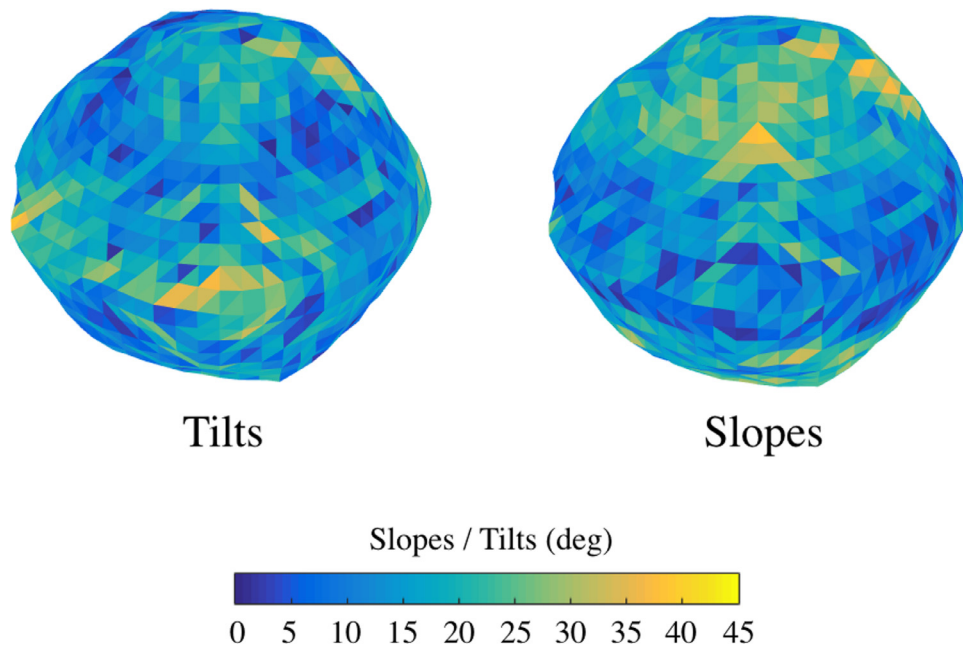


Fig. 8. Tilt and slope angles mapped across the Benu surface. Slopes are computed for the nominal density.

increase of the geopotential (defined as “downhill”) are in fact directly correlated. Thus the word “slope” can refer to both the inertial orientation of the surface and the direction of greatest increase in the geopotential. This is no longer the case on small bodies with a significant component of their geopotential energy arising from the rotation of the body. In fact, using a single term for the inertial orientation of a surface patch and the naturally measured “slope” of that surface is not appropriate.

As OSIRIS-REx must descend to the surface and sample it, the clear definition of these terms is crucial. Specifically, we define and distinguish between the orientation of the asteroid surface, the direction of greatest change in the geopotential and the relative measure of the geopotential across the surface. To distinguish between these concepts we introduce the terminology “Geometric Topography” and “Geopotential Topography.”

Geometric Topography. The geometric topography of the body is defined in terms of relative changes in the radius of the body (measured from the coordinate center) and in terms of the orientation of the surface relative to the vector from the coordinate center (note, we assume that the surface is locally star convex). The first is defined as geometric altitude, shown in Fig. 7 on the left. The surface orientation at a point on the surface is defined as the direction the normal vector to the surface at that location points, specified in a body-fixed frame. For a given location this can be defined as two angles. Let us take the radius vector of the surface location as a defining direction (assumed to be based at the body center of mass). The angle between the surface normal and the radius vector (extended through the surface) is defined as the “tilt” angle of that location (see Fig. 8, left). For a sphere the tilt angle will be uniformly zero. The local orientation of the normal

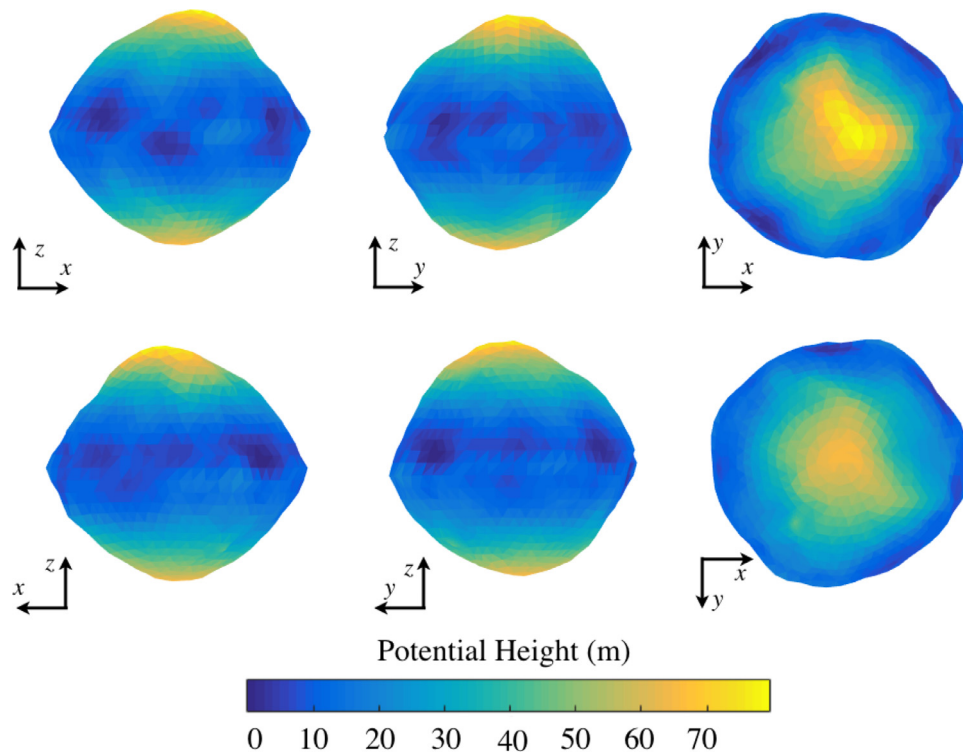


Fig. 9. Relative altitude computed across the surface of Benu at the nominal density, measured from the lowest geopotential value on the surface.

vector about the radius vector can be specified as the clock angle, measured in the tangent plane clockwise from the maximum moment of inertia axis of the body. These two angles, defined at a specific location on the asteroid surface, describe how that surface is oriented in the body frame, allowing it to be oriented in the inertial frame. This purely geometric quantity is important as a descending spacecraft will in general want to orient itself relative to this direction if it desires to make contact normal to the surface.

Geopotential Topography. The geopotential topography of the body is defined in terms of relative changes in the geopotential of the body and in terms of the orientation of the surface relative to the acceleration vector from the geopotential. The first is defined as the geopotential altitude, shown in Fig. 7 on the right (and defined below). The surface slope is defined as the relative orientation between the surface normal vector and the local acceleration vector (the gradient of the geopotential). The slope angle is defined as the supplement of the angle between the surface normal and the total acceleration vector at a given location. It is zero if they are oriented in opposite directions, and reaches 90° when perpendicular. The projection of the acceleration vector into the tangent plane to the surface defines the surface slope vector, and indicates the direction which an unconstrained particle would move if released from rest.

It is important to note that the surface tilt and slope can be quite different from each other, as shown in Fig. 8. This figure shows the Benu surface with the tilt angle and the slope angle (for the nominal density). These are not the same at all on the surface of Benu, due to the relatively large rotation rate of the asteroid. An analogous comparison for the Earth would show, however, that these two have a consistent direction and that their values are proportional (not equal because of the Earth's overall oblateness, which is rather small however).

4.2. Specifying the geopotential on the surface

A key application of the geopotential is to measure the relative energy of different locations on the surface. For planetary applications this is often done relative to an effective altitude of the locations above some reference “sea-level” height. This can be done at Benu, although the expressions of altitude may not be particularly meaningful. An alternate and perhaps more meaningful way to express relative energy involves the speed that would be gained for pure motion between two locations on the body. For completeness both are presented.

4.2.1. Geopotential altitude

A simple way to define the geopotential altitude is presented in the following (Turcotte and Schubert, 2014). First, define a specified value of the geopotential across the surface of the asteroid, and take this as a “sea-level” value. This can be the average value on the surface or more simply the lowest value across the surface. Next, measure the geopotential value at a given location relative to this reference, and divide by the local total acceleration of the geopotential at the given location. This provides an effective altitude in units of length. Fig. 9 shows this mapped across Benu for the nominal density.

The total variation of this measure of altitude is 79 m, although this variation changes if instead of the lowest value of the geopotential the altitude is made relative to the average geopotential value on the surface. From a geometrical perspective, this can be compared with the total variation in radius of the Benu model of 60 m from minimum to maximum radius. These differ due to the large variations in surface gravity across Benu. The change in altitude can be associated, approximately, with the amount of work required to move an object from one altitude to a higher altitude. Given this definition, the total change in altitude across Benu also varies as a function of the density. For the lowest density the total

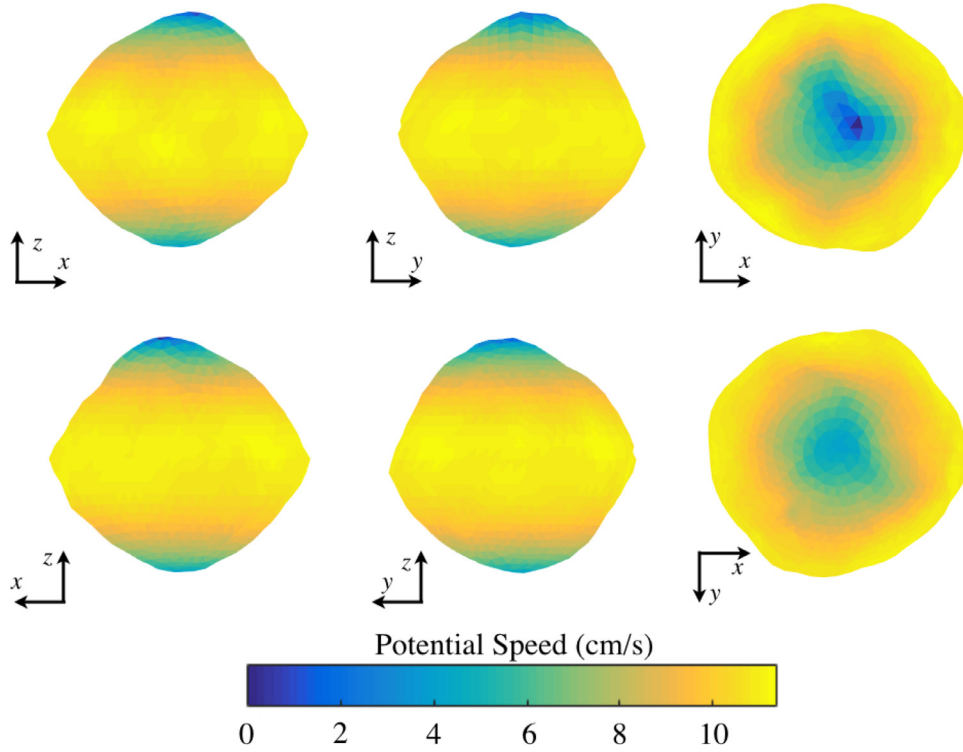


Fig. 10. Relative Jacobi speeds Δv_j computed across the surface of Benu.

change is 92 m, 79 m for the nominal and 71 m for the maximum density, relative large changes given the small size of this asteroid.

4.2.2. Jacobi speeds

A more dynamically meaningful and intuitive interpretation of the geopotential is in terms of the motion of particles relative to the body. Recall the Jacobi integral defined above in Eq. (9), which relates the speed of a particle with the geopotential value at its location and its Jacobi constant. What this relation tells us can be illustrated with a simple example. A particle that is thrown from the surface \mathbf{r}^* with a speed v^* will have an “energy” $C^* = \frac{1}{2}v^{*2} + V(\mathbf{r}^*)$ and when it lands at a different location on the surface \mathbf{r}' it will then have a speed $v' = \sqrt{2C^* - 2V(\mathbf{r}')} = \sqrt{v^{*2} - 2(V(\mathbf{r}') - V(\mathbf{r}^*))}$. Thus, the geopotential can be used to relate the relative energy between two points on the surface of a body. Specifically, if one takes $v^* = 0$ then this expression shows whether motion from one point \mathbf{r}^* to another point \mathbf{r}' is possible or not – if the expression within the square root is positive then motion between these locations is possible while if it is negative motion between them is not possible.

With this simple concept it is possible to map out the relative energy across the surface of the asteroid and identify the lowest and highest geopotential locations in the body and express their differences in terms of a dynamically relevant speed that a particle would gain or lose in traveling between such regions. This is defined as the “Jacobi speed” as a function of location on an asteroid as $v_j = \sqrt{-2V(\mathbf{r})}$, which can be plotted across the surface of an asteroid. In terms of this expression, the maximum value of v_j is the lowest geopotential point in the body. The relative values of the Jacobi speed across a body define the maximum speed which can be attained by a particle moving ballistically from one point to another.

Define $v_j^m = \min_{\mathbf{r} \in \partial B} v_j(\mathbf{r})$, which then defines the highest point in the geopotential. Then

$$\Delta v_j(\mathbf{r}) = \sqrt{v_j(\mathbf{r})^2 - v_j^{m2}} \quad (13)$$

is the amount of speed that a particle would gain in going from the highest point in the geopotential to the location \mathbf{r} , or conversely would be the speed a particle would require at a point \mathbf{r} to reach the highest point in the geopotential. This speed should be compared with the escape speed (defined later in Section 4.5) to evaluate whether a particle could achieve escape or orbit just based on its downslope motion on the body. Fig. 10 plots the value Δv_j across the surface of Benu for the nominal density. Note that the qualitative pattern of speeds does not change drastically with the density, although the overall magnitude of speeds increases with an increase in density. Specifically, the total variation of speeds across the surface of Benu is 11.1 cm s^{-1} for the low density, 11.4 cm s^{-1} for the nominal and 11.6 cm s^{-1} for the high density, a much smaller total variation across the range than found for the altitude. The maximum geopotential lies at the polar regions of the body while the minimum geopotential lies at the equator, in direct agreement with the relative height map. This is a common phenomenon for rapidly rotating bodies and has been predicted theoretically (Guibout and Scheeres, 2003) and shown to occur in specific asteroids, such as 1999 KW4 (Scheeres et al., 2006). The relative Jacobi speed between two points on the surface, \mathbf{r}' and \mathbf{r} , can be computed from $\sqrt{v_j(\mathbf{r}')^2 - v_j(\mathbf{r})^2}$ (assuming the points are arranged so that the quantity in the square root is positive).

4.3. Surface accelerations

Given the geopotential, an immediate application is to compute the accelerations on the surface of the body, as these will affect the flow and migration of disturbed materials and can be used to predict sites of regolith accumulation suitable for surface sampling.

Surface Accelerations at Different Densities

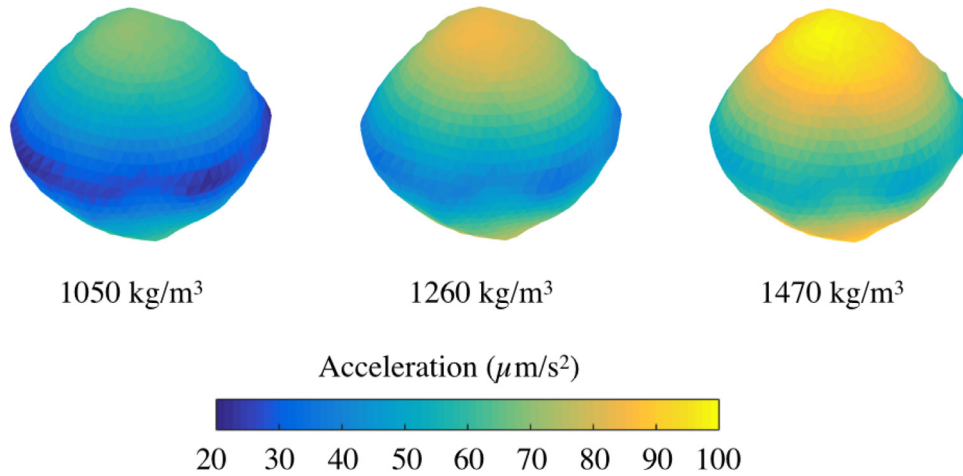


Fig. 11. Total acceleration across Bennu across the range of expected densities. Note that it is less than 10 microG and inward everywhere.

Given a point \mathbf{r} on the surface of the body the total acceleration in the body-fixed frame is the negative gradient of the geopotential $-\partial V/\partial \mathbf{r}$ evaluated at that point. This comprises a vector with a direction that points inward across the surface of Bennu, but which may have a significant deviation relative to its orientation to the surface (note that some bodies have accelerations that point away from the body, in particular 1950 DA (Rozitis et al., 2014)). Fig. 11 plots the total acceleration across the surface of Bennu, showing it from a particular vantage point for the three different densities.

These results show a consistent trend with the acceleration being minimized at the equator and maximized at the poles. This is directly due to the competition between the gravitational and centripetal accelerations and is inverted from the geopotential values. For each density the minimum and maximum accelerations are about $50 \mu\text{m s}^{-2}$ apart, constituting a factor of 2.5 variation for the lowest density and a factor of about 1 in variation for the highest density. Thus the total accelerations are highly sensitive to the density of the body. Regardless of this, the total magnitudes of the accelerations are quite small, being less than $100 \mu\text{m s}^{-2}$ (less than 10^{-5} Earth gravity) everywhere.

4.4. Surface slopes

The relationship between surface accelerations and the surface orientation give rise to the definition of surface slopes and their direction. The surface slope is defined as the supplement to the angle between the surface normal and the total acceleration vector (as computed from the geopotential gradient). Thus, the slope equals zero if the two are anti-aligned and is greater than or equal to 90° if the net acceleration is away from the surface. The slope analysis includes an evaluation of what Bennu's historical slopes may have been and if the shape encodes any evidence of a past rapid spin rate.

The slope vector is defined as the direction of the total acceleration vector projected into the local tangent plane. In simple terms, this defines the direction of sliding motion a particle would experience if moving downhill in the asteroid frame. If the slope is zero, this vector is zero, and is in general non-zero for all other values of slope up to 90° . When the slope is greater than this limit the slope vector is no longer well defined, as the natural motion of a particle would be to leave the surface of the body.

Figs. 12 and 13 show slope angles and slope vectors mapped over the surface of Bennu for the nominal density. In the com-

putation scheme, the total acceleration and surface normal are computed at the center of each triangular facet on the body and the slope and slope vector are computed at that point (Scheeres, 2012b). The slopes for the nominal density are uniformly less than 45° , with the current maximum slopes occurring in the mid-latitudes of the northern and southern hemispheres and with the equatorial region having the lowest slopes in general. Fig. 13 shows a characteristic pattern of the equatorial region being the downslope direction, with both north and south hemispheres preferentially moving material towards this region. This is to be expected as the equatorial region was seen to be the geopotential low of the asteroid surface.

The current shape of the asteroid can also be used to probe possible past rotation rates of the body. As developed in Scheeres (2015) the spin rate and bulk density of the body can be combined into a single parameter that correlates precisely with the slope distributions across the body (assuming a constant density mass distribution). This parameter is a non-dimensional rotation rate and equals

$$\tilde{\omega} = \frac{\omega}{\sqrt{\frac{4\pi}{3} G \sigma}} \quad (14)$$

where ω is the spin rate, G is the gravitational constant and σ is the bulk density. This is just the ratio of the asteroid spin rate over the mean motion of an object orbiting a spherical asteroid of density σ evaluated at its surface. In the ideal case, a sphere with $\tilde{\omega} > 1$ will have slopes of 180° at its equator as they would be feeling a net outward acceleration. This parameter also controls the slopes of a constant density body spinning about a fixed axis. For non-spherical shaped bodies the condition for equatorial lift-off usually occurs at values of $\tilde{\omega} < 1$ due to the extension of the body equator beyond the mean radius.

It is instructive to compute the values of $\tilde{\omega}$ for the current Bennu spin rate, assuming different values of density. These are listed in Table 5. In addition, larger values of $\tilde{\omega}$ have been computed to find the point where portions of the surface experience a net outward surface acceleration. Following Scheeres (2015) this provides a possible limit on the past spin rate of the body. Further, if at this spin rate extensive regions of near-constant slope are found it could be indicative of a past surface failure at this spin rate. For Bennu this limit was found to be approximately $\tilde{\omega} = 0.9$. In Table 5 the spin rate for this condition for each assumed density

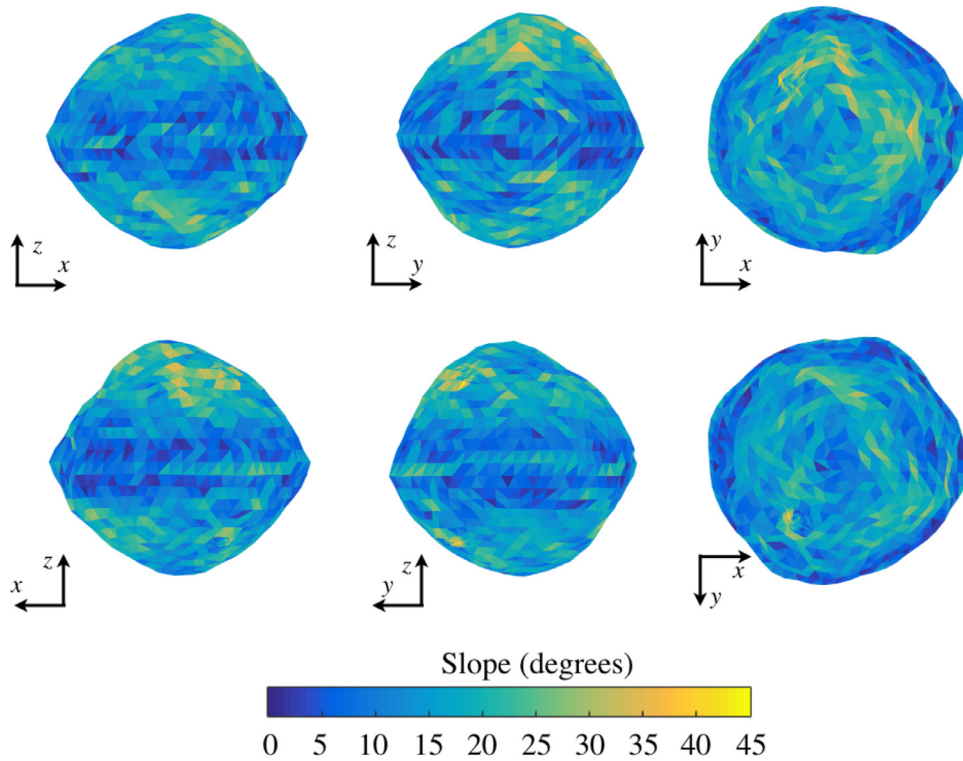


Fig. 12. Slopes mapped over the Bennu surface for the nominal density.

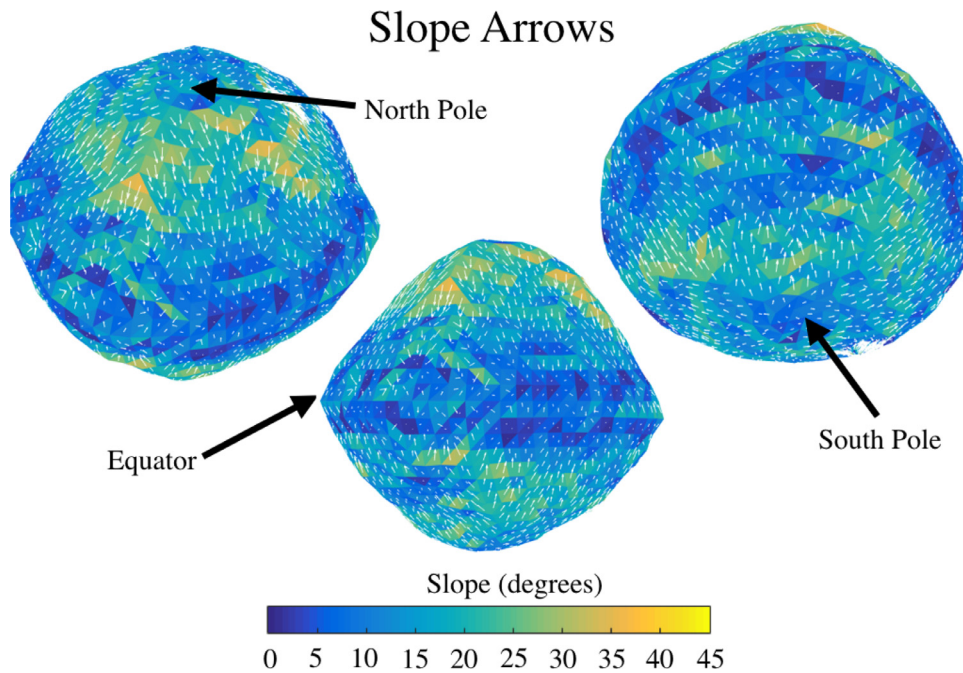


Fig. 13. Slopes arrows mapped over the Bennu surface for the nominal density as viewed from three different vantage points.

Table 5
Values of $\tilde{\omega}$ for different densities and the current Bennu spin period of 4.297812 h. Limiting spin periods are computed for $\tilde{\omega} = 0.9$.

Density (kg m ⁻³)	Current $\tilde{\omega}$ (-)	Limiting spin period (h)
1050	0.750	3.6
1260	0.684	3.3
1470	0.634	3.0

is also given. Note that this analysis assumes that the body density is constant for a range of spin rate variations.

Fig. 14 graphically shows the nominal density slope distribution at a range of faster spin rates. At 3.3 h the slopes are strongly focused about a limiting slope value of 35°, which is concentrated along the mid-latitudes of the body. This may indicate surface slope failures at a past point in time when, due to the YORP effect, the asteroid could have been spinning at a faster rate. At higher spin rates the slopes exceed 90° and their distribution becomes

Slopes at Limiting Spin Rates

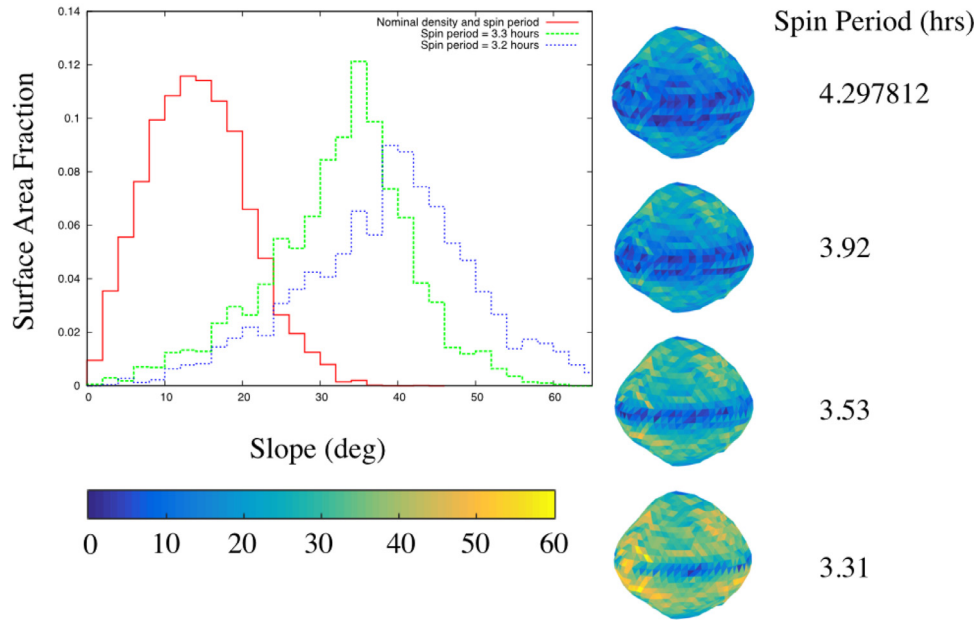


Fig. 14. Slope maps and distributions for different spin rates, assuming the nominal constant density.

more spread out. Such limits are not definitive, however, and the interpretation of such spin limits is highly dependent on the assumed strength of the asteroid's regolith covering and sub-surface, and is discussed later.

There is spectral information that circumstantially points to this limit having been reached or exceeded. Binzel et al. (2015) show evidence for the equatorial ridge of Bennu having a redder spectral slope than the poles, which may indicate finer grain sizes at the equator. A consistent explanation is rapid spin-up resulting in loss of larger particles (cm-scale and larger) where only the finest fraction grain sizes are held in place by cohesive forces. A resulting dominance of fine grains at the equator would create higher spectral slopes tentatively detected by Earth-based telescopic measurements preferentially viewing equatorial latitudes.

4.5. Surface escape speeds

Next, considering motion away from the surface of the body, the next computation to present is the escape speed mapped over the surface of the asteroid. This computation mixes the spin rate, surface orientation (or tilt) and total gravity field of the system together to develop a computation of the speed necessary to escape from the asteroid surface when ejected normal to the surface. For elongated bodies there can be a significant difference between leading and trailing edges of the spinning body, however these are usually subdued for spheroidally shaped bodies such as Bennu. Fig. 15 shows escape speeds mapped onto the asteroid surface for the nominal density, computed as described in Scheeres (2012b). There are some local regions of low and high escape speed, which correspond to the surface having a local tilt (see earlier definition in Section 4.1) in the leading or trailing direction, respectively. It is significant to note that the escape speeds across the body are all larger than the speeds attainable for disturbed grains that migrate to the equator, as can be inferred from Fig. 10. The difference between these at the equator is less than 3 cm s^{-1} . These are “guaranteed” escape speeds and only imply that the trajectory is initially on a hyperbolic escape orbit from the body.

This is an important distinction as it is still possible for a particle launched from the surface at lower speeds to achieve orbit and subsequently escape after an extended period of orbital motion about the asteroid. Surface speeds in this regime are difficult to distinguish, as the dynamical motion is chaotic, meaning that slight shifts in initial conditions of a particle lofted from the surface may result in drastically different dynamical evolutions. In some situations it is possible to place a lower limit on surface speeds, below which escape from the system is impossible (ignoring non-gravitational forces). This analysis is done by identifying the relative equilibria about a body and evaluating the geopotential limits associated with these. This approach is covered in more detail in Section 4.6. Fig. 16 plots what are called the return speeds across the surface of Bennu for the nominal density. A particle on the surface moving below this speed cannot escape from the asteroid. For bodies such as Bennu, with a spherical shape and rapid spin rate, there are large regions at mid to upper latitudes where escape is always possible for a particle dislodged from the surface (discussed in more detail in Scheeres (2015)). Note that a particle dislodged from the pole can achieve a speed of up to 11 cm s^{-1} (as inferred from Fig. 10), which is less than the guaranteed escape speed (Fig. 15) yet is greater than the return speed (Fig. 16), meaning that it is possible for particles displaced from the pole to enter orbit and eventually escape from the Bennu sphere of influence.

4.6. Close orbital environment

The influence of the geopotential does not end at the asteroid surface and continues into the space about the body as well. Here, it is most physically relevant to consider motion and dynamics in a frame that is fixed in and rotates with the body. In this frame there are special points where the gravitational attraction and centripetal acceleration are balanced, resulting in orbits that remain fixed in the rotating frame. These are known as equilibrium points in this rotating frame and can be used to evaluate limits on motion and the stability of motion in close proximity to the asteroid (Scheeres, 2012b). These are of geophysical interest as they can define the return speed limits for when particles can physically escape the

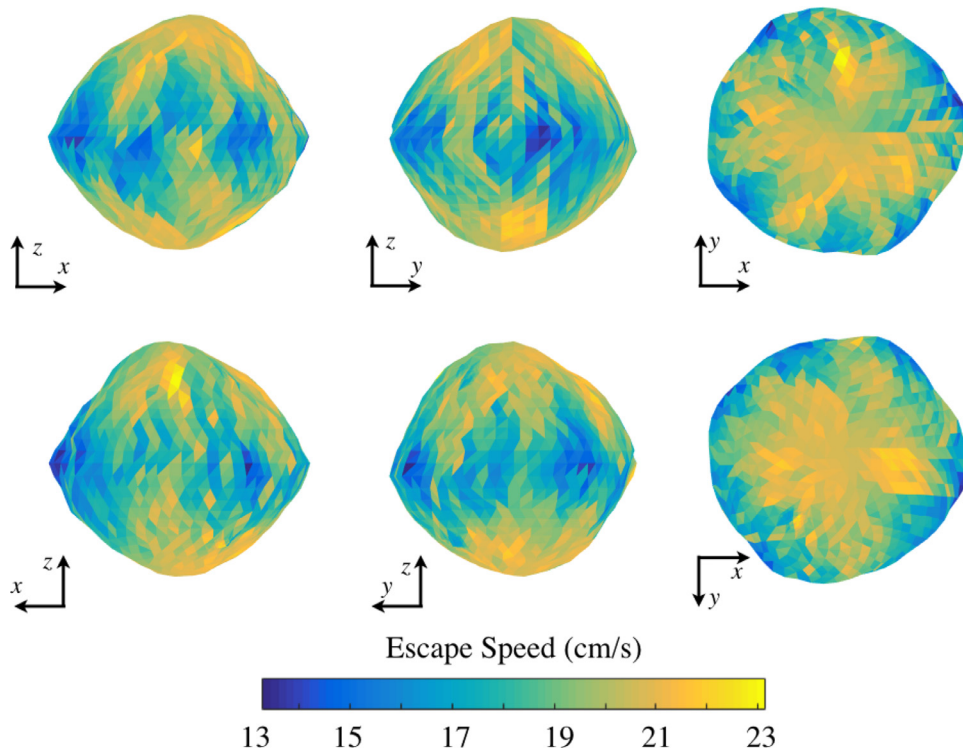


Fig. 15. Guaranteed escape speeds mapped over the asteroid surface, assuming the nominal constant density.

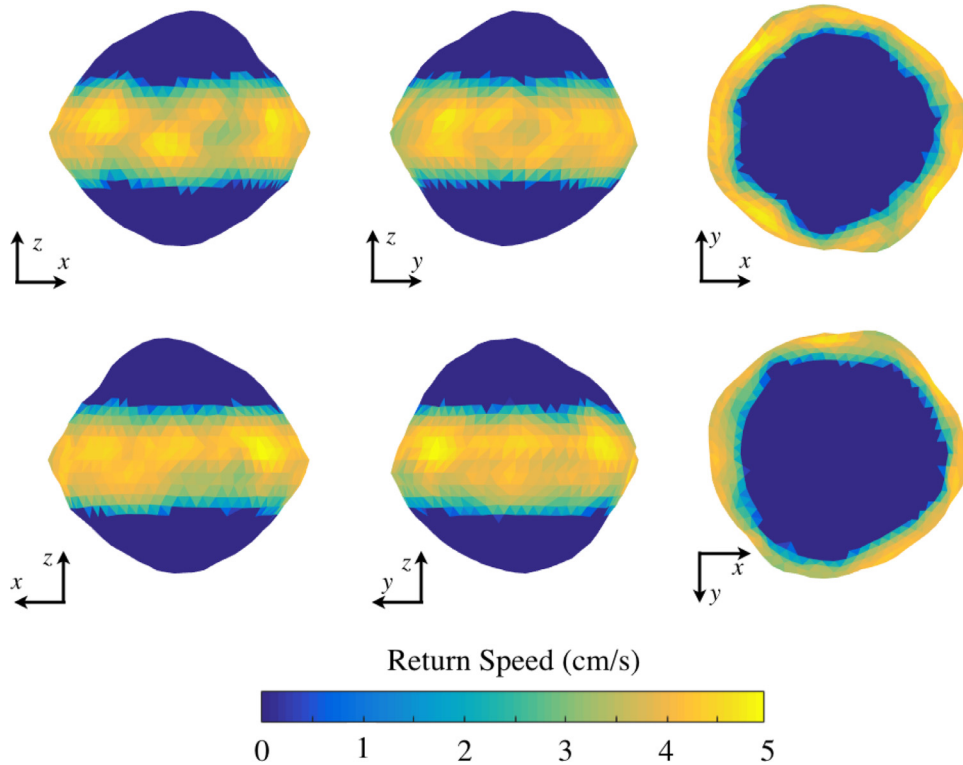


Fig. 16. Return speeds mapped over Benu, assuming the nominal constant density.

proximity of the asteroid, can be used to describe the motion of particles lofted above the surface and can be integrally tied to the evolution of asteroid shapes (Scheeres, 2015).

Equilibrium points are computed by solving the equation $\partial V / \partial \mathbf{r} = \mathbf{0}$, which has three conditions and three unknowns (the components of the position vector in the body-fixed frame). The

computation of these points and the determination of their stability properties are reviewed in Scheeres (2012b). Suffice it to say that these equilibrium points can either be stable or unstable. If they are classified as unstable, then relative motion in their vicinity will in general increase exponentially in time. They may either reimpact with the asteroid surface or drift farther away from

Pole-down view of Bennu showing the Equilibria

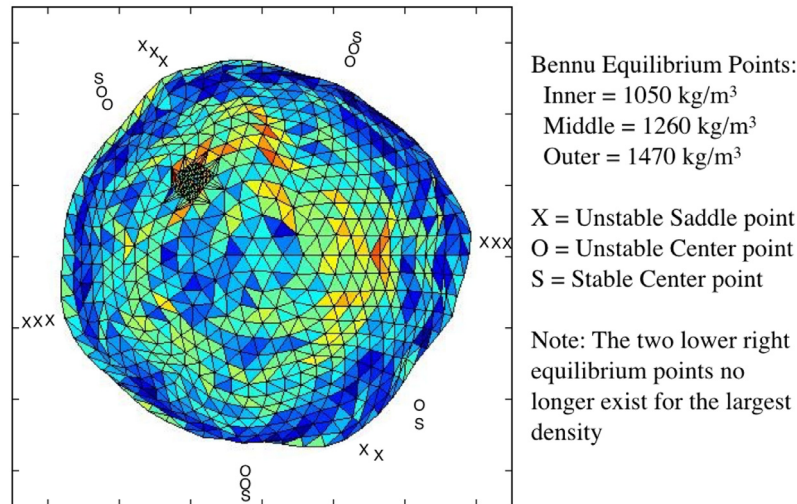


Fig. 17. Equilibrium points about Bennu at different densities. The stability properties and existence of these points is sensitive to the density and shape of the central body.

the body where they can either become trapped in orbit or escape from the system. The presence of some of these equilibrium points can in fact define mathematically rigorous limits on motion for a given energy, and can be used to show whether particles are trapped close to the asteroid surface or whether they are free to escape. Conversely, if an equilibrium point is found to be stable, then motion started in its vicinity will oscillate in its vicinity for some time period. Even in these cases, the motion of the particle will in general eventually leave the vicinity of the equilibrium point if acted on by non-gravitational forces or effects, although this can take a longer period of time, up to days or months for a body like Bennu.

Fig. 17 presents a summary of the equilibrium points found for the system at the limits of the densities. There are two types of unstable equilibrium points, saddle and center, with the distinction being that unstable center equilibrium points may become stable if the spin rate is reduced or the density increased (i.e., if $\tilde{\omega}$ is decreased). There are a few important characteristics of these equilibrium points. First, for lower densities there are more equilibrium points. The result is that when the density increases, the distance of the equilibria from the body center increases, which sometimes causes two equilibria to intersect and bifurcate out of existence. It is evident that this occurs as the nominal- and low-density cases have 8 distinct equilibria while the high density case only has 6.

Second, the low-density case has all of its equilibrium points unstable. This result means that at this limit any particles lofted from the surface, or placed there with low speed relative to the rotating body, will be unstable and will impact the body surface or drift to higher radii over a short time span of a few hours to a day. At the nominal density value, however, there is one stable center equilibrium point, and at the highest density there are three stable center equilibrium points. In these cases a particle lofted or placed in the vicinity of these locations may be stable and remain in orbit within a constrained region above the asteroid surface for an indefinite period of time.

Although stable, it is not expected to find long-term stable satellites in these locations as under energy-dissipation effects they tend to drift inward or outward. However, after a sampling operation at the asteroid it is possible to place a number of small particles and dust grains into orbits that would persist over periods of time long enough to potentially be of concern to the operations cadence of OSIRIS-REx, should multiple sampling attempts be necessary. From an observational point of view, if there are such sta-

ble equilibria at Bennu one might expect to see a concentration of dust and gravels distributed on the asteroid surface in the vicinity of these regions, as impact may cause lofted regolith to be captured into these regions from which they would migrate and impact on certain regions of the asteroid surface. As an example computation, Fig. 18 shows the trajectory of a particle lofted from the surface with a speed of less than 5 cm s⁻¹, traveling near to and becoming temporarily trapped around the stable equilibrium point region, and then falling back to the surface with a similar speed as it was lofted with. The total timespan of this trajectory is 5 days, or over 27 rotation periods of Bennu (meaning that it made over 27 orbits in inertial space before reimpacting). It is easy to find such ballistic transfers of even longer duration.

Additional context and understanding of the roles that these equilibrium points play in controlling the near-surface environment can be found by carrying out systematic computations and evaluations of these cases. Following the systematic procedure outlined in Tardivel (2014), Tardivel, 2014, the equilibria, manifolds, geopotentials and zero-acceleration surfaces for Bennu were computed for the different density values. These are shown in Fig. 19. Each figure shows the equilibrium points and the boundary of the potential attached to the point with the highest energy. This potential boundary is a geometrical curve that defines the dynamical barrier that separates motion outside of the curve with motion inside of the curve, with the two regions intersecting at the equilibrium point with largest energy. A particle with energy equal to or less than this value will either be trapped inside or outside of this curve. Also shown is the h^* section (defined as the surface at which the radial acceleration in a normal direction from the rotation pole is zero) that intersects with the z^* plane (defined as the surface at which the acceleration along the rotation pole is zero). This defines the radius at which the outward centripetal acceleration is equal to the inward gravitational acceleration in a direction normal to the rotation pole, evaluated along the curve where the out-of-plane accelerations are balanced and equal to zero. All of the equilibrium points lie along this curve, at angular locations where the transverse acceleration is equal to zero. Any particle in the body-fixed frame that is extended beyond this point will fall away from the asteroid, and conversely any particle within this curve in the asteroid frame will fall inward back to the surface.

The images along the top row show the relative values of the geopotential in the body-fixed frame. The brown regions are areas where the geopotential energy is more than the energy of the

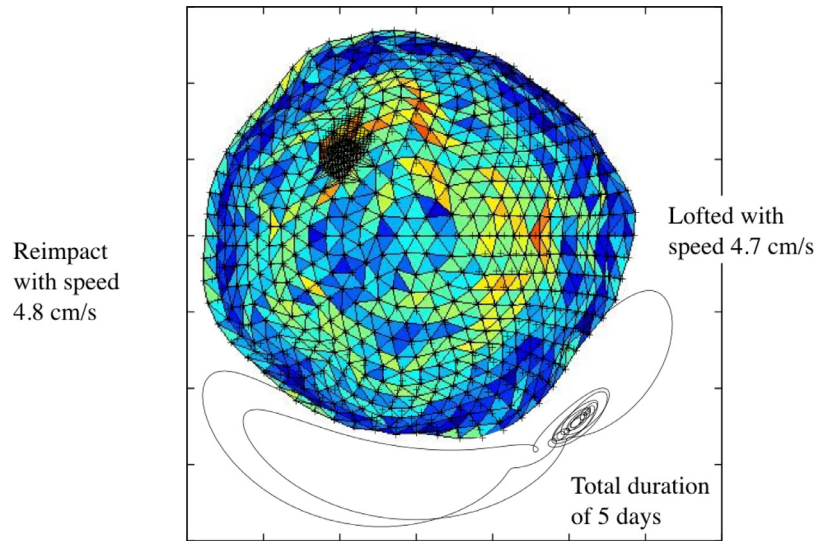


Fig. 18. A ballistic transfer across the surface of Bennu. The particle is lofted and impacts with a speed less than 5 cm s^{-1} and completes over 27 orbits in inertial space before reimpacting 5 days after being lofted. The body-relative speed during its period of being trapped close to the equilibrium point is less than 0.05 cm s^{-1} .

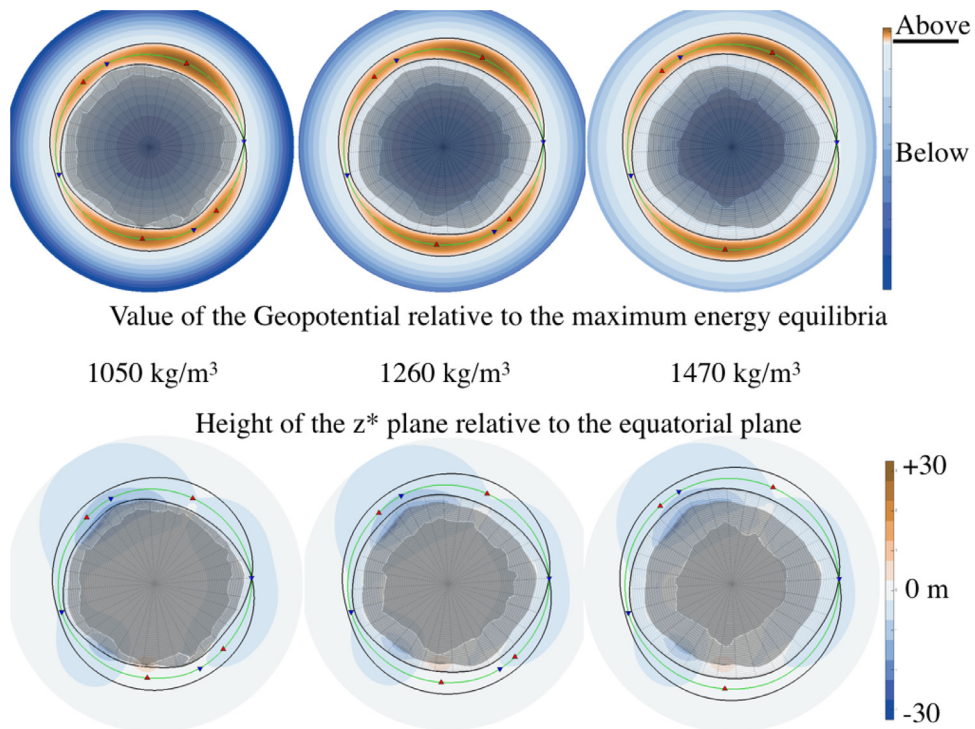


Fig. 19. Survey of dynamical structures for Bennu at different density values. See text for definitions.

equilibrium point with highest energy, and thus are regions that are unallowed for a particle with that energy to travel. The images along the bottom row have the equilibria, potential boundary and h^* curves overlain on contours of the out-of-plane distance between the $z = 0$ plane and the point where the north-south gravitational accelerations are balanced (the z^* surface). These distances range between -30 and $+5 \text{ m}$ and are mostly negative. This indicates a strong north-south effective asymmetry in the current shape model.

Fig. 20 shows the equilibrium point and h^* structure just below and beyond the spin rates at which the equilibrium points touch the surface. The points where the equilibria touch the surface are the regions where surface material will first feel an outward acceleration. If the surface material is cohesionless one would expect

a loss of material at these regions (Hirabayashi and Scheeres, 2014; Scheeres, 2015). The entire interior of the body does not experience an outward acceleration when the equilibrium point crosses into the body, which is what occurs for ideal constant density spheres and ellipsoids spun to this rate. Rather, just localized regions around the body experience this, and thus there are still attractive regions within the body although there are also some expansive regions wherever the h^* curve lies within the body.

4.7. Roche Lobe

Given the equilibrium points it is possible to compute the Roche Lobe of the asteroid. The Roche Lobe is defined as the

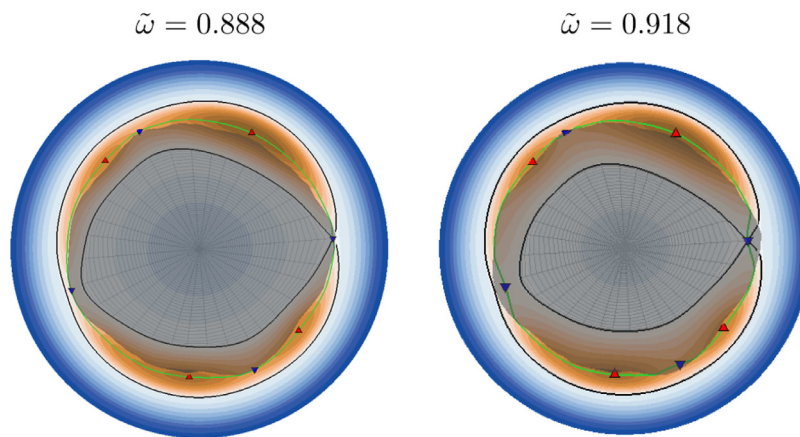


Fig. 20. Equilibrium point and h^* curve structure at the limiting spin rates and nominal density, as viewed from the North pole of Benu.

Roche Lobe at Benu

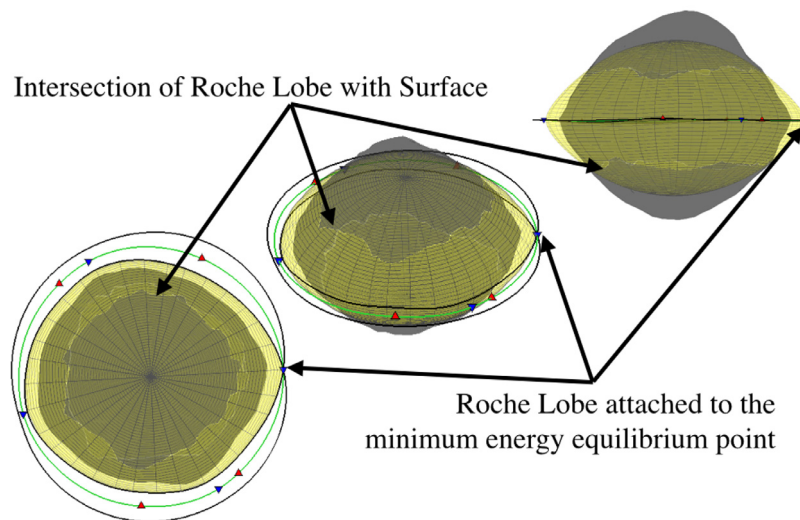


Fig. 21. Roche Lobe for Benu at its nominal density. Note the intersection between the lobe and the asteroid surface and its attachment to the equilibrium point. Triangles denote equilibrium points and the green line defines where the out-of-plane and radial accelerations are simultaneously equal to zero.

surface of the geopotential that has the same energy value as the minimum equilibrium point. Fig. 21 shows this surface for the nominal density case. There are a number of items that tie this surface back to some of the previously introduced concepts. First, the surface is evidently smooth everywhere except at the point where it attaches to the equilibrium point. This arises as the equilibrium point is a singular point of the Roche Lobe. Next, the intersection of the lobe with the Benu surface is coincident with the limits of non-zero return speeds seen in Fig. 16.

The Roche Lobe delineates the region around the asteroid from which stationary points are energetically bound to the body's vicinity. For the spheroidal, fast spinning bodies the lobe is generally seen to intersect with the body (Scheeres, 2015). This means that particles at higher latitudes have sufficient energy to enter orbit and escape from the asteroid if dislodged from their location. The process for this to occur would require them to slide down towards the equator where they would accumulate sufficient speed to leave the surface and enter orbit with sufficient energy for the zero-velocity surface to be open. Obviously, dissipative processes such as friction or impacts could decrease the particle's energy to the point where it is trapped again within this lobe. The speeds given in Fig. 16 correspond to the energy at which escape is no longer possible. The surface slopes (cf. Fig. 12) seem to

change their distribution characteristics around the intersection of the Roche Lobe with the surface, which could indicate the trapping of material in this region.

4.8. Internal stress state

Given the Benu shape model and density it is also possible to analyze the stress state of this body, using some assumed geophysical parameters such as friction angle and cohesion, which have a major influence on how and when the body can fail. The body is modeled with both a Drucker–Prager and Mohr–Coulomb failure theory, each of these being appropriate for describing granular material, which Benu is assumed to consist of due to its high porosity. The body is analyzed using several techniques, including modeling it as an ellipsoid, performing a global averaging analysis using its actual shape, and by analyzing it with a finite element method approach that captures the plastic deformation of the body. The techniques used are outlined in Hirabayashi and Scheeres (2014; 2015) and have been used to analyze the stress states of other bodies.

This analysis assumed a friction angle of 35° Lambe and Whitman (1969) which is typical for geological materials and explored the relationship between failure, cohesion and spin rate. Recent

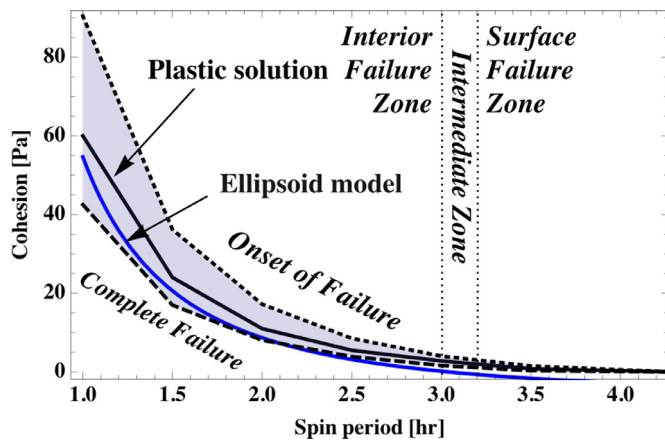


Fig. 22. Necessary levels of cohesion as a function of spin period to avoid failure for Benu. See Scheeres et al. (2015) and the text for definitions and descriptions.

theories for the evolution of rubble-pile bodies have indicated that some amount of cohesion within a rubble-pile body may be an important contributor to their overall evolution (Sánchez and Scheeres, 2014; Scheeres et al., 2015; 2010). The main result of cohesion within a rubble-pile is to control the conditions under which the surface or interior of the body will undergo plastic deformation and failure. Specifically, given fixed geophysical parameters it is possible to determine the level of cohesion necessary within a rubble-pile to withstand plastic deformation and failure as a function of current spin rate.

Fig. 22 shows the level of cohesion necessary to control failure of the body at a range of spin rates. The upper dotted and lower dashed lines are given using limit analysis applied to the full Benu shape model. The upper dotted line gives the highest level of cohesion needed such that Benu will not undergo failure. The lower dashed line gives the lowest level of cohesion, beneath which Benu would undergo plastic failure, potentially catastrophic. The black, upper solid line represents the necessary level of cohesion to avoid a catastrophic failure as determined by using plastic solutions from a commercial finite element software, ANSYS, version 15.03. This line is always between the dashed and dotted lines, implying the consistency of the models. The smooth solid line is from the averaged technique applied to an ellipsoid model (Holsapple, 2007). For a rubble-pile body with cohesion there are two main failure modes that can occur. At slow spin rates and low levels of cohesion it is possible for the body to fail due to surface landslides, as is shown in Fig. 23 on the left. At higher spin rates and stronger levels of cohesion the failure mode shifts from surface disruption to failure of the core, as shown in Fig. 23 on the right. These failure modes can be adjusted if the body has non-homogeneous distribution of strength, density or porosity properties (Hirabayashi, 2014; Hirabayashi et al., 2015).

Cohesion has recently been determined to be a key parameter for the strength of rubble-pile bodies (Scheeres et al., 2015), with theoretical studies and observations supporting the existence of a non-zero value for rubble piles. The genesis of such cohesion is still unknown, although there are specific theories for how it could arise from van der Waals forces between finer grains distributed throughout a rubble-pile body (discussed in more detail in Scheeres et al. (2015)). However, the level of cohesion that may exist within rubble-piles has only been weakly constrained to date, with published estimates and constraints from observations of asteroids ranging over a few orders of magnitude from ~25 Pa to a few hundred Pa (Hirabayashi et al., 2014; Rozitis et al., 2014; Sánchez and Scheeres, 2014). Further, possible values as a function of asteroid type and mineralogy are unexplored to date. At a co-

hesive strength of 25 Pa Benu would need to spin at a period of less than 2 h in order to undergo failure. This result is to be contrasted with the surface slope analysis presented earlier, which assumes cohesionless material, that indicated that the body would be subject to tensile loads when spinning faster than 3.2 h. To resolve these issues will require the detailed mapping of the Benu surface and interior to identify evidence for motion of surface material or the failure of the interior of the body. These details and future observations are discussed in the following.

5. Theories of Benu's shape

There are a number of current theories that have been proposed which could explain the shape of Benu, and in particular its equatorial ridge. These are reviewed in brief here as this is one of the main current questions raised by the existing data on Benu. Of course, there are many other questions of geophysical interest, and these will assuredly only increase once high-resolution measurements of the asteroid are made. However, we focus on this specific question now due to its unambiguous statement and larger interest, given the many bodies seen with radar shape models that have equatorial ridges (Benner et al., 2015). Most of these theories can be tied to specific physical predictions of mass or material morphology at this body. Thus these predictions are listed when appropriate as they may be the pathway to establishing the true cause of this body's shape. At their core, most of the theories can be evaluated or discriminated by a combination of asteroid surface morphology and a determination of the nature of internal density distribution.

5.1. Formation by landslides

Perhaps the most obvious theory is that the ridge region was formed by landslides of surface regolith traveling down to the equatorial region of this body. This can be directly inferred by noting that the geopotential low of the body – and hence all the slopes – lead directly to this region. This general theory was initially motivated by abstract studies of slope distributions and the energetics of stable configurations of material on ellipsoids (Guibout and Scheeres, 2003; Scheeres, 2007) and especially by the observed shape and geophysical properties of 1999 KW4 (Scheeres et al., 2006). Motivated by these observations there have been a number of analytical and numerical studies focused on how such surface flow mechanics should work. Analytical studies have focused on the conditions under which granular materials will flow, and how this flow can modify and influence the environment where they are emplaced (Harris et al., 2009; Minton, 2008; Scheeres, 2015). Numerical studies have approached the problem with the use of discrete element method codes (Hirabayashi et al., 2015; Sánchez and Scheeres, 2012; Walsh et al., 2008, 2012). In Walsh et al. (2008); 2012) it was found that surface landsliding could result in the formation of binary systems. In Sánchez and Scheeres (2012) it was found that the shape of the initial aggregate strongly controlled the mode of failure. Analytical work (Hirabayashi, 2014; Holsapple, 2004; Scheeres, 2015) and more recently numerical simulations (Hirabayashi et al., 2015; Walsh et al., 2012) have shown that for surface landsliding to globally occur prior to the internal failure of the body, however, the interior of the body must be stronger than the surface material. Note that this does not preclude local landslides due to initially high slopes. The genesis of this strength can either be differences in relative cohesion, density and packing, or even the angle of friction. In Hirabayashi et al. (2015) they show the degree to which the interior should be stronger for failure in terms of surface landsliding.

To establish this as the ridge-formation mode would require evidence for landsliding of surface material. This could be inferred by

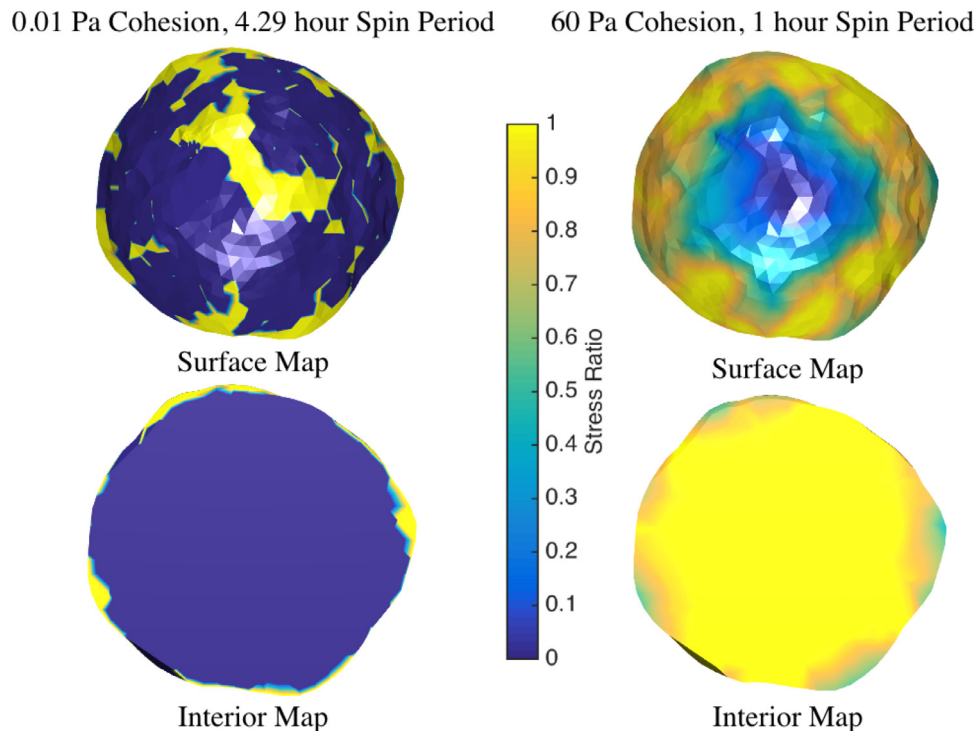


Fig. 23. Maps showing surface and interior failure modes for models of Bennu with nominal density. Left shows surface failure for low cohesion values at its current spin period. Right shows interior failure for higher cohesion values at a more rapid spin period. Regions at the top of the scale are undergoing plastic failure, while darker colors are further from failure conditions. The figures look down on the positive spin axis and the Interior Maps are a cross section through the equatorial plane.

a few different observations. Foremost, it should be evident morphologically by identifying pathways of flow from mid-latitudinal regions towards the equatorial region. A similar analysis was performed in Miyamoto et al. (2007) which established the flow direction of regolith on Itokawa. One would expect to see regions of the surface at slope failure limits (potentially for faster spin periods, as discussed above in Section 4.4). From Harris et al. (2009), Scheeres (2015) these regions would be at mid-latitudes, as this is where the maximum slopes on a spinning spheroidal body lie. There would also be an expected accumulation of material at the ridge location, potentially being truncated at a given radius defined by the Roche Lobe at the faster spin period where failure would be suspected of occurring (Scheeres, 2015), which would be evident from the detailed shape model.

Finally, there should be two possible aspects of density inhomogeneity that could indicate this failure mode as well. First, as noted above, the interior of the body must be stronger than the surface for this landsliding to occur. This property could be correlated with an increased density in the interior region, as the main mode for increased strength within a rubble-pile body would be a more compressed (i.e., lower porosity) interior which would lead to a higher density. In addition, granular material that flows generally undergoes dilation, meaning that it becomes more porous as it flows. This is linked to its plastic failure mode and physically arises as flowing material must arrange itself with higher porosity for grains to move relative to each other. This dual contrast, higher-density interior and lower-density ridge could provide supporting evidence for this mode of failure as well. In this regard it is significant to note that the geopotential low of Bennu does not exist within a confined space but actually exists at the top of a ridge (which is counter to the usual situation on Earth where geopotential lows will lie within depressions). Thus, it is not necessarily expected that the material which flows downslope to this region will be compacted and thus could retain its high porosity.

5.2. Infall of fissioned material

A second possible formation mode for the equatorial ridge is also linked to the formation of binary asteroid systems. In this mode the ridge would be formed from the infall of material that was fissioned off of the parent body. This was initially proposed in Scheeres et al. (2006) as one possible explanation for the equatorial ridge of 1999 KW4 and was further explored in Jacobson and Scheeres (2011) in connection with the coupled orbital and rotational dynamics of a binary asteroid system following fission (Pravec et al., 2010). In this mode the symmetry of the equatorial ridge arises as the infall material is either distributed symmetrically prior to infall (such as in a temporary ring or disc system that collapses on the surface) or the infall material (which could still be comprised of a size distribution) is distributed longitudinally as it strikes the surface at a higher relative speed (but still much less than escape speed). For this scenario to play out there must first have been a fission of material from the body, and then subsequent infall from the rotationally disrupted secondary (Jacobson and Scheeres, 2011) or the infall of a debris disc (Scheeres et al., 2006).

Given this detailed sequence of formation events as motivation, evidence of both events should be present for this to be tagged as an unambiguous outcome. Fission of material would be evident from the detailed shape model and its surface morphology and spectral properties, and should in general leave a record of one region being exposed or otherwise disturbed over a significant area of the surface of the body. The evidence for infall could arise from the morphology of the ridge itself, especially if it is seen to not be connected to surface flows from the mid-latitudes, but instead to have the appearance of being layered on top of the existing surface. This mode of failure does not make any strong predictions for density inhomogeneity, in that it is not even clear whether the infall of material onto the equatorial ridge would tend to compact

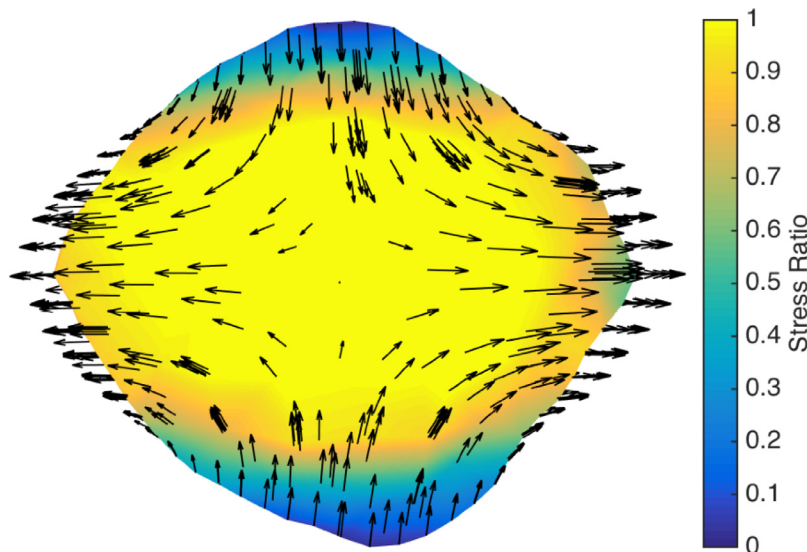


Fig. 24. Cross-section of Bennu showing patterns for plastic deformation and flow for the interior failure case. Material moves most strongly horizontally in the equatorial direction, which could create the observed equatorial ridge.

the granular matter or allow it to settle in a high-porosity case. Additionally, the onset of fission is linked to homogeneous density distributions (Hirabayashi et al., 2015) or weaker (and potentially less dense) interiors. It is significant to note that evidence for fission should also be linked to the global flow of granular material and potentially localized density inhomogeneities. Thus, should any evidence for such a failure mode be seen it would be a natural target for the investigation of density inhomogeneity.

5.3. Failure of the internal core

A third mode of formation has been identified more recently (Hirabayashi and Scheeres, 2015). If a body has some cohesive strength which is homogeneously distributed through the rubble-pile, then it will fail from the interior first. This was analyzed in detail for the asteroid 1950 DA and is a natural conclusion from the general theory of plastic deformation in the presence of strength (Holsapple, 2007). In this failure mode, the interior undergoes a plastic deformation whose failure mode naturally propagates outward along the equatorial plane of the body (see Fig. 24). This process would create a more porous center of the body while compressing the material that constitutes the ridge. This failure mode can occur prior to the surface being placed into tension, although it would be more efficient if the body is overspinning. What is unknown, and can be investigated in more detail, is whether there should be a corresponding failure of material along the polar dimension due solely to gravitational attraction that would potentially compress the core again. This phenomenon would depend in part on the cohesive strength of the rubble-pile material and the total density of the distribution.

In this model, evidence for this failure mode would again be a combination of shape and surface morphology, with the potential addition of density inhomogeneity measurements. The equatorial ridge itself in this model would appear as an uplift that moves away from the spin axis and could extend to higher latitudes, depending on the degree of deformation that occurs. This action would be expected to either compress or maintain the surface and sub-surface porosity, while the interior porosity would in general be expected to increase due to the flow of material. Again, the combination of surface morphology and flow with an underdense core would provide supporting evidence for this mode of failure.

6. Geophysically relevant measurements

The OSIRIS-REx mission will measure several key elements for understanding the geophysical environment. These are described in general in the following, along with an example calculation that shows how some of these geophysical quantities of interest can be determined.

6.1. Bennu shape

The OSIRIS-REx mission will obtain the shape of Bennu using two independent approaches that will be undertaken in parallel. The first approach makes use of stereophotoclinometry (SPC) (Gaskell et al., 2008). SPC was first developed in the mid-to-late 1980s to generate the topography of Io using Voyager data. More recently SPC has been employed to successfully develop the shape of asteroids Eros, Vesta and Itokawa, the comet 67P/Churyumov-Gerasimenko, and the planet Mercury, using rendezvous mission data. It was a key element to producing the shapes of the asteroids Lutetia and Steins during the flyby of those targets. SPC uses imagery obtained of the surface of an asteroid, preferably collected at a range of emission and incidence angles. The technique combines stereo with photoclinometry to derive the tilt of an asteroid's surface. Stereo provides excellent estimates of the position of a suite of individual landmarks across a given surface, and allows estimating a relationship between surface tilt and observed albedo. With this relationship in hand, the tilts of a piece of asteroid surface imaged at multiple emission and incidence angles can be obtained via least squares that best duplicates the overlapping input images. Once surface tilts are determined, heights across each map can be determined by integrating over the tilts to produce the shape of the surface within high fidelity regional "maplets" surrounding each landmark (see Fig. 25). These individual maps of the surface shape are then collated together to produce a shape model. SPC uses as additional constraints asteroid limb and terminator data to help further improve the global shape of an asteroid or comet.

The second approach makes use of data acquired by the OSIRIS-REx laser altimeter (OLA). Developed by the Canadian Space Agency, OLA will operate when the OSIRIS-REx spacecraft is < 7 km from Bennu. OLA will be the first scanning laser altimeter to fly on a planetary mission and is capable of acquiring raster scans in two dimensions of the surface of Bennu at separate times

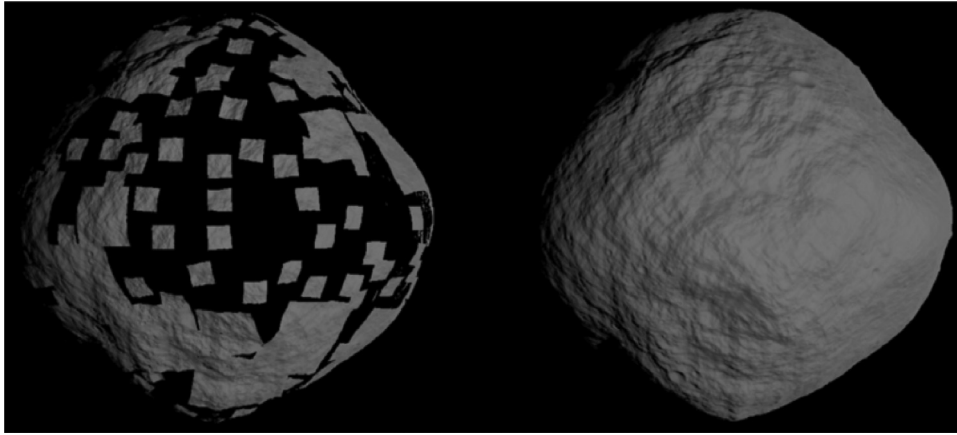


Fig. 25. Lefthand side shows SPC local maplets that are combined together to generate high resolution global and local shape models of the surface of Bennu. Data are from a test using simulated images obtained from a simulated Bennu shape model.

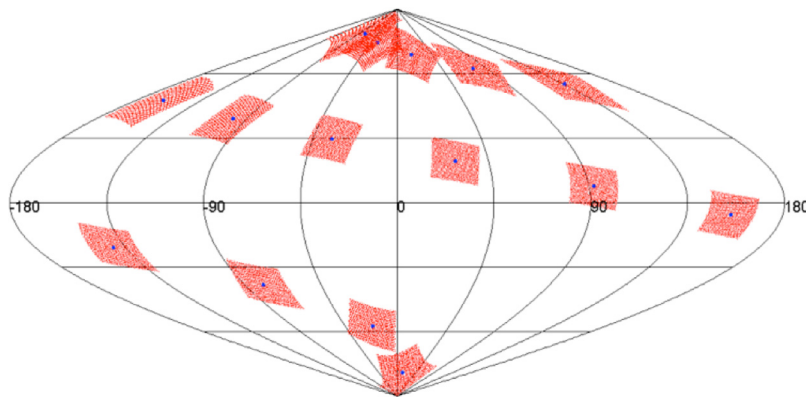


Fig. 26. Sinusoidal projection of where simulated OLA raster scans will be acquired on the surface of Bennu after one day of observation. These raster scans will be patched together to estimate precisely the asteroid shape.

in orbit, much as a framing camera would be operated during any typical planetary mission (see Fig. 26). When assembled these scans can generate a very accurate global shape model of the asteroid, as well as precise information on the position of the spacecraft relative to Bennu whenever an OLA raster is acquired.

The current best estimate of the accuracy of the shape models produced by SPC will be 35 cm globally, and 5 cm for regional sites where OSIRIS-REx expects to sample the surface of the asteroid. OLA products will be comparable or better in accuracy; indeed, some preliminary tests indicate that the OLA shape model could possess accuracies < 5 cm. Accuracy is defined as the RMS uncertainty associated with the known location of each piece of Bennu terrain from the center of figure of the asteroid. The vertical precision of the surface of Bennu, which is the vertical RMS difference between individual surface elements, will be known to < 2.5 cm.

These global measurement accuracies are of much higher quality than anything obtained before at an asteroid, and will enable existing theories to be tested and new discoveries of how the surface of an asteroid such as Bennu has evolved. For comparison, Itokawa's surface is at best known to an accuracy of a meter globally and Eros' to decameters globally. Specifically, these accuracies will make it possible, when joined with the estimated gravity field, to provide evidence for regolith flow that might have been produced by a suite of possible geophysical processes as mentioned previously. Their location, scale and associations with slope relative to gravity and topographic elevation will be critical for testing which one of these myriad of processes might be the most important in producing the observed Bennu geology. These data will also make it possible to assess debris aprons around large blocks,

or assess the slopes near the edge of regolith pond deposits, which might or might not embay and cover surrounding terrain. These latter measurements will be key to constraining the importance of surface cohesiveness in shaping Bennu.

6.2. Surface morphology

The distribution, orientations and physical properties of rocks and boulders on Bennu may indicate numerous geologic processes – including material flows across the surface. There is evidence on asteroids Eros and Lutetia of fine particle movement (e.g., Mantz et al., 2004; Thomas et al., 2012), and asteroid Itokawa has fine grains segregated to gravitational potential lows and numerous signs of landslide-like material flows based on particle distributions and orientations (Miyamoto et al., 2007).

The planned imaging campaign at Bennu will achieve resolution on order of 20 cm globally, and as detailed as 2 cm for two potential sampling sites. Organization of rocks and boulders can indicate past flow and imbrication (alignment of axes) can help to determine the direction of flow. The physical properties of observed rocks and boulders (rounded or jagged and angular) may indicate processing due to micrometeorite impacts, spin-up and disruption processes or thermal fatigue and exfoliation (Connolly et al., 2015; Delbo et al., 2014), or they may indicate processing prior to incorporation in a rubble pile (Marshall and Rizk, 2015). The comprehensive imaging will also survey linear features that may track surface flows directly. Similarly, should craters exist on Bennu, their distribution and stratigraphy relative to different geologic regions,

will provide valuable context in interpreting the history of the asteroid.

Combined, the geologic context of boulder properties and distributions along with other observed and mapped features will construct a larger context of the surface history – including the geophysics relative to the equatorial ridge.

In addition to optical imaging, the surface of Bennu will be observed in the thermal infra-red with the OTES instrument at multiple local solar times (Hamilton and Christensen, 2014). These data will allow for determination of thermal inertia across the surface, which provides information on the porosity and grain size of the regolith. Relative changes in thermal inertia will then be investigated in light of observed surface morphology to determine whether certain regions show signs of greater or lesser porosity. This correlation can, in turn, be used to understand any flow features evident on the surface of the asteroid.

The thermal inertia of potential sample sites will be mapped at higher spatial resolution (8 m or better). The thermal inertia information will be combined with data from other instruments to determine surface grain size, porosity, and composition. The high-resolution imaging and information from the Touch-and-Go sampling events (see Lauretta, 2015) will allow for more detailed insight into the correlation between thermal inertia and grain size at specific locations on the Bennu surface. This analysis may allow for a partial calibration of the thermal inertia data across the global Bennu surface.

6.3. Gravity field

Knowledge of the gravity field allows one to infer details about the distribution of mass within Bennu, which otherwise cannot be sensed with the instruments available on OSIRIS-REx. The gravity field will mainly be measured through the Radio Science experiment, which is carried out over a 9-day arc of quiescent spacecraft operations from the 1-km radius terminator orbit. Over the course of this 9-day period, the telecommunication system will gather nearly continuous Doppler tracking of the spacecraft, along with a significant number of optical navigation images and lidar ranges, to precisely track the trajectory of the spacecraft around Bennu. This data set is then used to estimate the gravity field of Bennu.

Current covariance analysis of this scenario indicates that the gravitation parameter, μ , and the first- and second-degree and order gravity coefficients can be estimated accurately. These parameters provide us with estimates of the total mass, from μ , the location of the center of mass within the body, from the 1st degree coefficients, and information about the moments of inertia of Bennu from the second-degree and order terms. According to these results, the mass will be estimated to approximately 0.025%, and the center of mass will be estimated to within 30 cm on each axis, both at the 3σ level. The accuracies of the moments of inertia are harder to state due to the fact that only the difference of the moments of inertia can be estimated from the gravity field data. However the second-degree and order gravity field is estimated to better than 10%, which will provide constraints on the moments of inertia. It should be noted that if Bennu is found to be in an excited rotation state, that it is then possible to also estimate the trace of the inertia tensor. This allows for the moments of inertia to be estimated by combining the observed rotational motion with the estimated gravitational coefficients. This would provide additional constraints on the mass distribution.

The third and higher-degree and order gravity field will be constrained by these data, but will be difficult to estimate accurately. In general, C_{30} , C_{31} , S_{31} , and C_{40} can be estimated accurately while the remaining higher degree terms are only weakly constrained by this data set for the current nominal plan.

6.4. Density

The bulk density and density distribution within Bennu are key estimates that will frame our understanding of this body. The bulk density is simply based on the estimated total mass of the asteroid divided by the volume of its shape model. The mass estimate is expected to be quite accurate (see above), and so it will be the volume uncertainties, expected to be less than 1%, that limit the accuracy of this determination. This result is used, in turn, to compute the porosity of the asteroid – defined as the fraction of void space within the asteroid's volume. To make this computation an estimate of the grain density of the asteroid is needed. This property will be accurately determined once the sample is returned to Earth and analyzed. The porosity will provide an initial indication of the mass-distribution morphology within the body, although it will not provide direct information on how the void spaces are distributed.

Constraints on the distribution of density within the asteroid will be a key item to be estimated. To do this the measured gravity field (and moments of inertia should Bennu be in a complex rotation state) must be compared to the constant-density gravity field determined from the asteroid's shape. This approach was used by the NEAR mission at asteroid Eros to determine that the interior of that body had a uniform density distribution (Miller et al., 2002). Disparities between the measured and computed constant-density gravity field coefficients can indicate the presence of a non-uniform density distribution within the body. To carry out the next step – which is to map out how the density is distributed – is more difficult.

There are a range of techniques that can be used for this analysis, summarized in Takahashi and Scheeres (2014a). In general, these approaches involve making a hypothesis for the morphology of density distribution and then testing it by fitting the relative densities of the different assumed components and comparing with the measured gravity field. This approach cannot provide an unambiguous result, but can be used to identify plausible internal distributions, and most recently has been used for constraining the Vesta interior (Park et al., 2014). The current discussion focuses on the simplest approach to this problem for definiteness; whether there is an over or under-dense core within the asteroid Bennu. Depending on the theory of geophysical evolution one may subscribe to, a prediction of either a relatively over or under-dense core can result, meaning that this measurement could be a crucial delimiter between competing theories. While more complex density inhomogeneities can be developed (as shown in Takahashi and Scheeres, 2014a), the effect of a spherical core of different density is by far the easiest to analyze and use as a motivation.

Assume that the estimated Bennu gravity field coefficients are denoted as C_{ij}^e and S_{ij}^e , where these are the coefficients of degree i and order j and are considered to be representative of the true gravity field coefficients. Current plans are to estimate these up to degree and order 4 for Bennu, although this is influenced by the actual mass of the body. The estimated gravity coefficients are to be compared with the gravity field coefficients calculated based on the asteroid shape and total mass, assuming a constant-density field, and denoted as C_{ij}^s and S_{ij}^s . Deviations in the density distribution from uniform will show up as differences between these sets of coefficients. Specifically, if the actual density distribution consists of a spherical core of radius R with a uniform density, and a different but uniform density value outside of this spherical core, then the difference between the estimated and constant density shape gravity coefficient equals

$$\Delta C_{ij} = -\frac{\Delta M_C}{M_T} C_{ij}^s \quad (15)$$

Table 6

Expected signal in relative density based on nominal measurement projections of the OSIRIS-REx radio science orbit.

R_C Radius (m)	$\Delta\sigma$ Density (kg m^{-3})	$\Delta\sigma/\sigma$ Relative density (-)
100	323	0.26
150	96	0.08
200	40	0.03

with a similar equation for ΔS_{ij} where $\Delta M_C = 4\pi/3\Delta\sigma R_C^3$ and is the excess or deficit mass of the spherical core with radius R_C and density deviation $\Delta\sigma$ from the total bulk density, and M_T is the total mass of the asteroid (Takahashi and Scheeres, 2014a).

Now consider the ability to measure such a density disparity, using the best measured gravity coefficient C_{20} as an example. Based on a nominal bulk density of 1260 kg m^{-3} and a 1-km Radio Science tracking orbit over 10 days the expected uncertainty in C_{20} is 2.7×10^{-4} for a nominal value of 1.75×10^{-2} , leading to a relative uncertainty $\sigma_{C_{20}}/C_{20} \sim 0.015$. This provides a prediction, as a function of core radius, of the precision to which the core density can be estimated (assuming of course that it is a spherical core). Table 6 presents the relative precision of this measurement as a function of the size of the core using the nominal density as the bulk density. This shows that a spherical core of radius 100 m can be detected, but that a core smaller than this with a fixed density variation will become progressively more difficult to detect based on the single gravity coefficient C_{20} (or conversely, that a smaller core must have a larger density variation to be detected). However, in this model all other gravity coefficients will be modified by the same factor, enabling their use to increase the precision of the determination and the ability to identify this particular mode.

7. Conclusions

This paper reviews current information on Asteroid (101955) Benu, the target asteroid of the OSIRIS-REx sample return mission. Using the currently estimated models for this asteroid a range of quantities of geophysical interest are computed for understanding this specific body. The current computations assume a uniform density for this body and provide the current best estimates for the geophysical state of this body. In addition, possible theories for the formation of the ridge on Benu are reviewed and ways in which these competing theories can be resolved based on measurements available to OSIRIS-REx during its rendezvous with Benu are identified. In addition to these discussions the projected accuracies to which key components of the asteroid can be measured or estimated are reviewed.

Acknowledgments

The research and writing of this paper was supported by NASA contract NNM10AA11C (D.S. Lauretta, PI) and related subcontracts from the University of Arizona. D. Farnocchia and S.R. Chesley conducted this research at the Jet Propulsion Laboratory, California Institute of Technology, under a contract with NASA. S. Tardivel acknowledges support by an appointment to the NASA Postdoctoral Program (NPP) at the Jet Propulsion Laboratory, California Institute of Technology, administered by Oak Ridge Associated Universities through a contract with NASA. P. Michel acknowledges support by

the French space agency CNES. M.G. Daly acknowledges support from the Canadian Space Agency.

References

- Abe, S., Mukai, T., Hirata, N., et al., 2006. Mass and local topography measurements of Itokawa by Hayabusa. *Science* 312 (5778), 1344–1347.
- Barnouin-Jha, O.S., Cheng, A.F., Mukai, T., et al., 2008. Small-scale topography of 25143 Itokawa from the Hayabusa laser altimeter. *Icarus* 198 (1), 108–124.
- Benner, L.A.M., Busch, M.W., Giorgini, J.D., et al., 2015. Radar observations of near-earth and main-belt asteroids. *Asteroids IV* 165–182.
- Binzel, R.P., DeMeo, F.E., Burt, B.J., et al., 2015. Spectral slope variations for OSIRIS-REx target asteroid (101955) Benu: possible evidence for a fine-grained regolith equatorial ridge. *Icarus* 256, 22–29.
- Botke, W.F., Vokrouhlický, D., Walsh, K.J., et al., 2015. In search of the source of asteroid (101955) Benu: applications of the stochastic YORP model. *Icarus* 247, 191–217.
- Breiter, S., Bartač, P., Czekaj, M., et al., 2009. The YORP effect on 25143 Itokawa. *Astron. Astrophys.* 507 (2), 1073.
- Broschart, S.B., Abrahamson, M., Bhaskaran, S., et al., February 2015. The small-body dynamics toolkit and associated close-proximity navigation analysis tools at JPL. In: 2015 AAS Guidance and Control Conference, Breckenridge, Colorado. Paper AAS 15-XXX.
- Cheng, A.F., Barnouin-Jha, O., Zuber, M.T., et al., April 2001. Laser altimetry of small-scale features on 433 Eros from NEAR-shoemaker. *Science* 292, 488–491.
- Chesley, S.R., Farnocchia, D., Nolan, M.C., et al., 2014. Orbit and bulk density of the OSIRIS-REx target asteroid (101955) Benu. *Icarus* 235, 5–22.
- Clark, B.E., Binzel, R.P., Howell, E.S., et al., 2011. Asteroid (101955) 1999 RQ36: spectroscopy from 0.4 to 2.4 μm and meteorite analogs. *Icarus* 216 (2), 462–475.
- Connolly Jr., H.C., Lauretta, D.S., Walsh, K.J., et al., 2015. Towards understanding the dynamical evolution of asteroid 25143 Itokawa: constraints from sample analysis. *Earth, Planets Space* 67 (1), 1–6.
- Delbo, M., Libourel, G., Wilkerson, J., et al., 2014. Thermal fatigue as the origin of regolith on small asteroids. *Nature* 508 (7495), 233–236.
- DeSouza, I., Daly, M.G., Barnouin, O.S., et al., February 2015. Improved techniques for size-frequency distribution analysis in the planetary sciences: application to blocks on 25143 Itokawa. *Icarus* 247, 77–80.
- Emery, J.P., Fernández, Y.R., Kelley, M.S.P., et al., 2014. Thermal infrared observations and thermophysical characterization of OSIRIS-REx target asteroid (101955) Benu. *Icarus* 234, 17–35.
- Fujiwara, A., Kawaguchi, J., Yeomans, D.K., et al., 2006. The rubble-pile asteroid Itokawa as observed by Hayabusa. *Science* 312 (5778), 1330–1334.
- Garmier, R., Barriot, J.P., Konopliv, A.S., et al., April 2002. Modeling of the Eros gravity field as an ellipsoidal harmonic expansion from the NEAR Doppler tracking data. *Geophys. Res. Lett.* 29 (8), 1231.
- Gaskell, R.W., Barnouin-Jha, O.S., Scheeres, D.J., et al., 2008. Characterizing and navigating small bodies with imaging data. *Meteorit. Planet. Sci.* 43 (6), 1049–1061.
- Geissler, P., Petit, J.M., Durda, D.D., et al., 1996. Erosion and ejecta reaccretion on 243 Ida and its moon. *Icarus* 120 (1), 140–157.
- Golubov, O., Krugly, Y.N., 2012. Tangential component of the YORP effect. *Astrophys. J. Lett.* 752 (1), L11.
- Golubov, O., Scheeres, D.J., Krugly, Y.N., 2014. A three-dimensional model of tangential YORP. *Astrophys. J.* 794 (1), 22.
- Guibout, V., Scheeres, D.J., November 2003. Stability of surface motion on a rotating ellipsoid. *Celestial Mech. Dyn. Astron.* 87, 263–290.
- Gundlach, B., Blum, J., 2013. A new method to determine the grain size of planetary regolith. *Icarus* 223 (1), 479–492.
- Hamilton, V., Christensen, P., 2014. The OSIRIS-REx thermal emission spectrometer (OTES). In: EGU General Assembly Conference Abstracts, vol. 16, p. 4687.
- Harris, A.W., Fahnestock, E.G., Pravec, P., 2009. On the shapes and spins of 'rubble pile' asteroids. *Icarus* 199 (2), 310–318.
- Hergenrother, C.W., Barucci, M.A., Barnouin, O., et al., 2014. The design reference asteroid for the OSIRIS-REx mission target (101955) Benu. arXiv:1409.4704
- Hergenrother, C.W., Nolan, M.C., Binzel, R.P., et al., 2013. Lightcurve, color and phase function photometry of the OSIRIS-REx target asteroid (101955) Benu. *Icarus* 226 (1), 663–670.
- Herrera-Sucarrat, E., Palmer, P.L., Roberts, R.M., 2013. Modeling the gravitational potential of a nonspherical asteroid. *J. Guidance Control Dyn.* 36 (3), 790–798.
- Hirabayashi, M., 2014. Structural failure of two-density-layer cohesionless biaxial ellipsoids. *Icarus* 236, 178–180.
- Hirabayashi, M., Sánchez, P., Scheeres, D.J., 2015. Internal structure of asteroids having surface shedding due to rotational instability. *Astrophys. J.* 808 (1), 63.
- Hirabayashi, M., Scheeres, D.J., 2014. Analysis of asteroid (216) Kleopatra using dynamical and structural constraints. *Astrophys. J.* 780 (2), 160.
- Hirabayashi, M., Scheeres, D.J., 2015. Stress and failure analysis of rapidly rotating asteroid (29075) 1950 DA. *Astrophys. J. Lett.* 798 (1), L8.
- Hirabayashi, M., Scheeres, D.J., Sánchez, D.P., et al., July 2014. Constraints on the physical properties of main belt comet p/2013 r3 from its breakup event. *ApJL* 789, L12.
- Holsapple, K.A., 2004. Equilibrium figures of spinning bodies with self-gravity. *Icarus* 172 (1), 272–303.
- Holsapple, K.A., April 2007. Spin limits of solar system bodies: from the small fast-rotators to 2003 EL61. *Icarus* 187, 500–509.
- Jacobson, S.A., Scheeres, D.J., July 2011. Dynamics of rotationally fissioned asteroids: source of observed small asteroid systems. *Icarus* 214, 161–178.

- Kaula, W.M., 1966. Theory of Satellite Geodesy. Applications of Satellites to Geodesy. Blaisdell, Waltham, MA.
- Konopliv, A.S., Miller, J.K., Owen, W.M., et al., December 2002. A global solution for the gravity field, rotation, landmarks, and ephemeris of Eros. *Icarus* 160, 289–299.
- Krugly, Y.N., Belskaya, I.N., Shevchenko, V.G., et al., 2002. The near-Earth objects follow-up program: IV. CCD photometry in 1996–1999. *Icarus* 158 (2), 294–304.
- Lambe, T.W., Whitman, R.V., 1969. Soil Mechanics. John Wiley & Sons.
- Lauretta, D.S., 2015. OSIRIS-REx asteroid sample-return mission. In: Handbook of Cosmic Hazards and Planetary Defense, pp. 543–567.
- Lauretta, D.S., Bartels, A.E., Barucci, M.A., et al., 2015. The OSIRIS-REx target asteroid (101955) Bennu: constraints on its physical, geological, and dynamical nature from astronomical observations. *Meteorit. Planet. Sci.* 50 (4), 834–849.
- Lowry, S.C., Weissman, P.R., Duddy, S.R., et al., 2014. The internal structure of asteroid (25143) Itokawa as revealed by detection of YORP spin-up. *Astron. Astrophys.* 562, A48.
- Manz, A., Sullivan, R., Veverka, J., 2004. Regolith transport in craters on Eros. *Icarus* 167 (1), 197–203.
- Marshall, J., Rizk, B., 2015. Rounded boulders on Itokawa as clues to geological processes in the early solar system. *Planet. Space Sci.* 119, 181–184.
- Mazrouei, S., Daly, M.G., Barnouin, O.S., et al., 2014. Block distributions on Itokawa. *Icarus* 229, 181–189.
- McMahon, J.W., Scheeres, D.J., Farnocchia, D., et al., August 2015. Optimizing small body gravity field estimation over short arcs. In: 2015 AAS/AIAA Astrodynamics Specialist Meeting, Vail, Colorado. Paper AAS 15-669.
- Michikami, T., Nakamura, A.M., Hirata, N., May 2010. The shape distribution of boulders on asteroid 25143 Itokawa: comparison with fragments from impact experiments. *Icarus* 207 (1), 277–284.
- Michikami, T., Nakamura, A.M., Hirata, N., et al., 2008. Size-frequency statistics of boulders on global surface of asteroid 25143 Itokawa. *Earth Planets Space* 60 (1), 13–20.
- Miller, J.K., Konopliv, A.S., Antreasian, P.G., et al., January 2002. Determination of shape, gravity, and rotational state of asteroid 433 Eros. *Icarus* 155, 3–17.
- Minton, D.A., 2008. The topographic limits of gravitationally bound, rotating sand piles. *Icarus* 195 (2), 698–704.
- Miyamoto, H., Yano, H., Scheeres, D.J., et al., May 2007. Regolith migration and sorting on asteroid Itokawa. *Science* 316, 1011.
- Nolan, M.C., Magri, C., Howell, E.S., et al., 2013. Shape model and surface properties of the OSIRIS-REx target asteroid (101955) Bennu from radar and lightcurve observations. *Icarus* 226 (1), 629–640.
- Noviello, J.L., Barnouin, C.M., Ernst, O.S., et al., 2014. Block distribution on Itokawa: implications for asteroid surface evolution. In: 45th Lunar and Planetary Science Conference, 45, p. 1587.
- Park, R.S., Konopliv, A.S., Asmar, S.W., et al., 2014. Gravity field expansion in ellipsoidal harmonic and polyhedral internal representations applied to Vesta. *Icarus* 240, 118–132.
- Pravec, P., Vokrouhlický, D., Polshook, D., et al., 2010. Formation of asteroid pairs by rotational fission. *Nature* 466 (7310), 1085–1088.
- Prockter, L., Thomas, P., Robinson, M., et al., 2002. Surface expressions of structural features on Eros. *Icarus* 155 (1), 75–93.
- Robinson, M.S., Thomas, P.C., Veverka, J., et al., 2002. The geology of 433 Eros. *Meteorit. Planet. Sci.* 37 (12), 1651–1684.
- Rozitis, B., MacLennan, E., Emery, J.P., 2014. Cohesive forces prevent the rotational breakup of rubble-pile asteroid (29075) 1950 DA. *Nature* 512 (7513), 174–176.
- Sánchez, P., Scheeres, D.J., 2012. DEM simulation of rotation-induced reshaping and disruption of rubble-pile asteroids. *Icarus* 218, 876–894.
- Sánchez, P., Scheeres, D.J., 2014. The strength of regolith and rubble pile asteroids. *Meteorit. Planet. Sci.* 49 (5), 788–811.
- Scheeres, D.J., 2007. Rotational fission of contact binary asteroids. *Icarus* 189 (2), 370–385.
- Scheeres, D.J., 2012a. Orbit mechanics about asteroids and comets. *J. Guidance Control Dyn.* 35 (3), 987–997.
- Scheeres, D.J., 2012b. Orbital Motion in Strongly Perturbed Environments: Applications to Asteroid, Comet and Planetary Satellite Orbiters. Springer-Praxis, London, UK.
- Scheeres, D.J., 2015. Landslides and mass shedding on spinning spheroidal asteroids. *Icarus* 247, 1–17.
- Scheeres, D.J., Abe, M., Yoshikawa, M., et al., 2007. The effect of YORP on Itokawa. *Icarus* 188 (2), 425–429.
- Scheeres, D.J., Britt, D., Carry, B., et al., 2015. Asteroid interiors and morphology. Asteroids IV. Univ. Arizona Press.
- Scheeres, D.J., Fahnestock, E.G., Ostro, S.J., et al., November 2006. Dynamical configuration of binary near-earth asteroid (66391) 1999 KW4. *Science* 314, 1280–1283.
- Scheeres, D.J., Gaskell, R.W., 2008. Effect of density inhomogeneity on YORP: the case of Itokawa. *Icarus* 198 (1), 125–129.
- Scheeres, D.J., Hartzell, C.M., Sánchez, P., et al., December 2010. Scaling forces to asteroid surfaces: the role of cohesion. *Icarus* 210, 968–984.
- Scheeres, D.J., Khushalani, B., Werner, R.A., August 2000. Estimating asteroid density distributions from shape and gravity information. *Planet. Space Sci.* 48, 965–971.
- Takahashi, Y., Scheeres, D.J., 2014a. Morphology driven density distribution estimation for small bodies. *Icarus* 233, 179–193.
- Takahashi, Y., Scheeres, D.J., 2014b. Small body surface gravity fields via spherical harmonic expansions. *Celestial Mech. Dyn. Astron.* 119 (2), 169–206.
- Takahashi, Y., Scheeres, D.J., Werner, R.A., 2013. Surface gravity fields for asteroids and comets. *J. Guidance Control Dyn.* 36 (2), 362–374.
- Tardivel, S., 2014. The Deployment of Scientific Packages to Asteroid Surfaces. University of Colorado Ph.D. thesis.
- Thomas, N., Barbieri, C., Keller, H.U., et al., 2012. The geomorphology of (21) Lutetia: results from the OSIRIS imaging system onboard ESA's Rosetta spacecraft. *Planet. Space Sci.* 66 (1), 96–124.
- Thomas, P.C., Robinson, M.S., July 2005. Seismic resurfacing by a single impact on the asteroid 433 Eros. *Nature* 436, 366–369.
- Tsuchiyama, A., Uesugi, M., Matsushima, T., et al., 2011. Three-dimensional structure of Hayabusa samples: origin and evolution of Itokawa regolith. *Science* 333 (6046), 1125–1128.
- Turcotte, D.L., Schubert, G., 2014. Geodynamics. Cambridge University Press.
- Veverka, J., Robinson, M., Thomas, P., et al., 2000. NEAR at Eros: imaging and spectral results. *Science* 289 (5487), 2088–2097.
- Ševeček, P., Brož, M., Čapek, D., et al., 2015. The thermal emission from boulders on (25143) Itokawa and general implications for the YORP effect. *Mon. Not. R. Astron. Soc.* 450 (2), 2104–2115.
- Walsh, K.J., Delbó, M., Bottke, W.F., et al., 2013. Introducing the Eulalia and new Polana asteroid families: re-assessing primitive asteroid families in the inner main belt. *Icarus* 225 (1), 283–297.
- Walsh, K.J., Richardson, D.C., Michel, P., 2008. Rotational breakup as the origin of small binary asteroids. *Nature* 454 (7201), 188–191.
- Walsh, K.J., Richardson, D.C., Michel, P., 2012. Spin-up of rubble-pile asteroids: disruption, satellite formation, and equilibrium shapes. *Icarus* 220 (2), 514–529.
- Werner, R.A., 1997. Spherical harmonic coefficients for the potential of a constant-density polyhedron. *Comput. Geosci.* 23 (10), 1071–1077.
- Werner, R.A., Scheeres, D.J., 1997. Exterior gravitation of a polyhedron derived and compared with harmonic and mascon gravitation representations of asteroid 4769 Castalia. *Celestial Mech. Dyn. Astron.* 65, 313–344.
- Yano, H., Kubota, T., Miyamoto, H., et al., 2006. Touchdown of the Hayabusa spacecraft at the muses sea on Itokawa. *Science* 312 (5778), 1350–1353.